Annual Progress Report

The Texas Center for High Intensity Laser Science and the The Texas Petawatt Project

2004

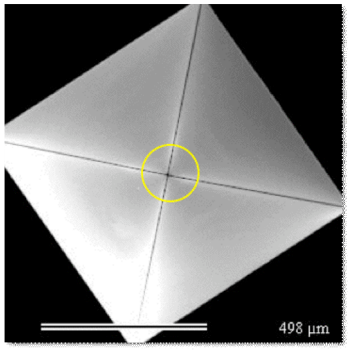

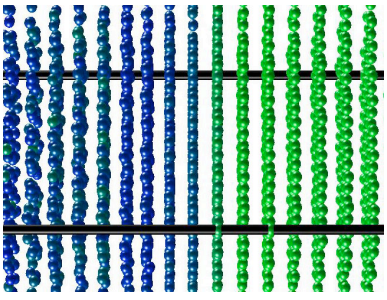

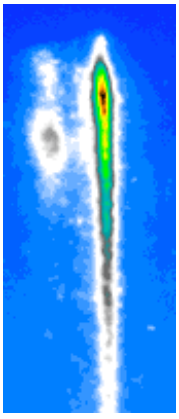

Annual Progress Report
for SSAA Cooperative agreement DE-FC52-03NA00156

The Texas Center for High Intensity Laser Science
The Texas Petawatt Project

Submitted by Todd Ditmire (Director of TCHILS, University of Texas at Austin)

I. Science activities at the Texas Center for High Intensity Laser Science

During the first full year of work under this SSAA Center, we have conducted a wide range of experiments. These experiments have utilized laser facilities at UT, LLNL, Sandia and the University of Michigan. The emphasis of research in the Center is based in two areas, high energy density physics, including hydrodynamics and high temperature plasma experiments, and high strain rate materials science. In addition, the Center has undertaken the construction of a Petawatt laser facility. This document describes each of the science activities in the Center as well as the activities in support of the Petawatt laser development. The individuals involved in each Center activity are listed under each sub-section.

Section I describes each of the science activities in the Center, section II discusses the laser development activities and section III lists the individuals supported by the SSAA Center grant and all the publications resulting from the funding of the Center to date.

I.A Radiative blast wave studies on the Sandia Z-Beamlet Laser and the UT THOR laser

Participants:
A. E. Edens, J. Osterhoff, D. R. Symes, and T. Ditmire (University of Texas)
J. F. Hansen and M. J. Edwards (Lawrence Livermore National Laboratory)
R.G. Adams, P. Rambo, L. Ruggles, I.C. Smith, and J. L. Porter (Sandia National Laboratory)

A central activity within the Center involves the study of hydrodynamic behavior of high Mach number blast waves. Our interest in these wave is based on the fact that very high velocity blast waves can become radiative and exhibit hydrodynamics instabilities. These experimental studies have been conducted on a number of laser facilities. We have performed experiments on the LLNL Janus laser and the Sandia Z-Beamlet laser. We have also performed experiments in slightly different geometry on the UT THOR laser.

Central to this work is the study of the stability of shock waves [1-4]. In particular, there are several instabilities of interest associated with the formation and evolution of shock waves produced by supernovae, i.e. supernova remnants(SNRs) [2,5]. One important hydrodynamic feature associated with some radiative SNRs, an overstability proposed by Vishniac et al., arises from a mismatch between the ram and thermal pressures at the surface of a blast wave which can cause a growing, oscillating ripple on that surface [3,6,7]. Radiative SNR shocks are cooler and

more compressible than non-radiative SNR shocks, leading to a thinner blast front which is susceptible to this Vishniac overstability [8-11]. Vishniac et al. made quantitative predictions for the temporal evolution of small perturbations on a blast wave front and derived the growth rate of the overstability as a function of the effective adiabatic index of the shocked material and wave number of the oscillation [7].Most experimental attempts to see the Vishniac overstability have used laser irradiation of a target to create a blast wave in a background gas [12,13]. These experiments take advantage of a laser's ability to deliver a large amount of energy to a small focal spot in a time span short compared to the evolution of the resulting explosion. There are several complications associated with these experiments that make it difficult to measure the growth rate of the overstability. The first complication for laser experiments in spherical geometry, as opposed to cylindrical geometry, is the effect of the laser's passage on the background gas, which can pre-ionize the gas. A second complication to experimental observation is that if the overstability grows from noise it is difficult to achieve large growth in the limited lifetime of the experiments.

Some of the data described here was acquired on the Z-Beamlet laser at Sandia National Laboratories [14], which fired 500J-1000J, 1ns pulses of 1054nm wavelength. The remainder of the data was taken on the Janus laser at Lawrence Livermore National Laboratory [15], which fired 10 J-150 J, 1ns laser pulses at 527nm wavelength. These pulses illuminated 500 micron diameter cylindrical solid targets immersed in 5-10 Torr of nitrogen or xenon gas. The resulting explosions created the blast waves that we studied. The setup used is diagramed in Figure I.A.1. The inset in this figure shows the main diagnostic employed: a dark-field telescope. This diagnostic is used in conjunction with a probe laser and is sensitive to density gradients, such as those that occur at the edge of a blast wave. The probe laser used with Z-Beamlet fired ~80 mJ, 150ps pulses at 1064nm. The probe laser used with Janus fired ~10mJ, 2ns pulses at 527nm. These lasers could be fired at a variable interval after the drive laser allowing us to examine the evolution of our blast wave over several microseconds. For part of the experiments, regularly spaced wire arrays were used to induce single frequency perturbations on blast waves. The wire array contained a square of open space approximately 3cm on a side through which 30 gauge tin-copper wire was strung. The wires were spaced 2, 4, or 6mm apart, corresponding to induced perturbations with spherical mode numbers of ~28, 14, and 9 given the size of the blast wave at the time it intersected the array.

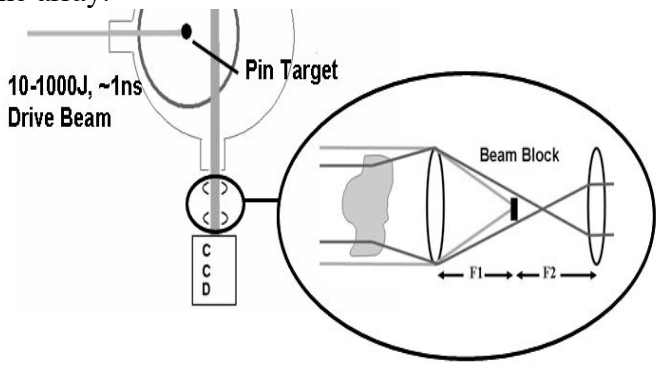

Figure I.A.1: Experimental setup for laser-produced blast wave experiments. The 10J-1000J, 1ns drive beam enters one side of the chamber, illuminating a 0.5mm solid target and creating a blast wave. A variable time later a probe laser is fired and comes in perpendicular to the drive beam, imaging the blast wave. Inset: Diagram of dark field telescope. Light that goes through the experiment undeflected gets blocked by a beam block at the focus of the imaging telescope. Deflected light shows up as a bright area on the CCD.

The first experiments were performed without the wire array and looked at the evolution of the radius of the blast wave as a function of time. The position of any feature of a blast wave, such as the blast wave front, will evolve as $R(t) = \xi t^{\alpha}$. Blast waves that do not lose or gain a significant fraction of their initial energy during their evolution, i.e. those where radiation does not play an important role in the hydrodynamics, follow the Taylor-Sedov solution, where α=0.4 [16]. In blast waves where radiation is important, a solution with a lower α will be followed, as the energy loss via radiation causes these blast waves to slow down more quickly. Therefore the trajectory of a blast wave can show the importance of radiation on its hydrodynamics.

Images of blast waves produced by 1000J laser pulses at various times along with a measured trajectory are shown in Figure I.A.2 with 10 Torr of nitrogen as the background gas and in Figure I.A.3 with 10 Torr of xenon as the background gas. The trajectory in nitrogen follows a $t^{0.4}$ trajectory to a high degree of accuracy over its entire history. In contrast, while xenon at late times (>400ns) may expand as $t^{0.4}$, at earlier times the trajectory appears to exhibit a lower α. This lower exponent most likely arises from the fact that energy losses via radiation have an effect on the hydrodynamics of the blast wave. Another indication that radiation plays a much larger role for blast waves in xenon than in those traveling through nitrogen is the radiative precursor. When a blast wave radiates, some of the energy is absorbed by the background gas, creating a heated, ionized region in front of the blast wave. This ionized region shows up as a bright area on the dark field images. In Figure I.A.2, while there is a noticeable glow surrounding the blast waves it is localized to the region immediately surrounding the blast wave, never extending more than 7 mm away from the edge of the blast wave. This can be contrasted with Figure I.A.3, where the precursor region extends off the field of view, at least several cm, demonstrating a significantly greater amount of radiation emitted from blast waves in xenon.

Another feature of note from these images is the presence of a "bump" feature on the laser side of the blast waves, especially those in xenon gas. A closer look at an example of this feature can be seen in Figure I.A.4. A qualitatively similar feature occurs for blast waves in xenon at all drive laser energies from 10J-1000J and always occurs along the path of the laser focal cone. This feature arises from the interaction of the laser with the background gas. As the laser passes through the background gas, it heats and ionizes the gas it passes through. This creates a warm, lower density channel of gas where the blast wave will travel faster than in other regions, which results in the bump like feature seen in the data. Simulations on this phenomenon were performed using CALE, the Lawrence Livermore National Laboratory 2-D arbitrary Lagrangian Eulerian (ALE) code with a tabular equation of state (EOS) and interface tracking [17]. They indicate that for a 100J drive laser pulse, the laser channel region is heated to up to 12eV, comparable to what we expect the temperature of the shock heated gas to be.

For the next set of experiments we placed wire arrays in the path of blast waves produced by 1000J laser pulses in order to induce perturbations. When we did this for blast waves traveling through xenon, the radiation from the blast wave ablated the wire array, creating secondary blast waves that interfered with our main blast wave until they were outside our field of view. The formation of these secondary blast waves is illustrated in Figure I.A5. For blast waves traveling through nitrogen, we expected that the induced perturbations would decay away over time. Because radiation does not appear to play an important role in the energy dynamics of these blast

waves, their blast fronts should be too thick for growth of the Vishniac overstability to occur. However, the radiative precursor around the nitrogen blast wave images in Figure I.A.2 indicates that some radiation is emitted, which could lower the effective adiabatic index somewhat, resulting in slightly thinner blast waves. The adiabatic index for a perfect monatomic gas is 1.66 and we would expect that our adiabatic index would be somewhere between this value and 1.2, the value where growth begins to occur for the Vishniac overstability. Some of the images corresponding to each of our wire arrays are shown in Figure I.A.6. In each case the induced perturbations clearly damp out, matching our intuition.

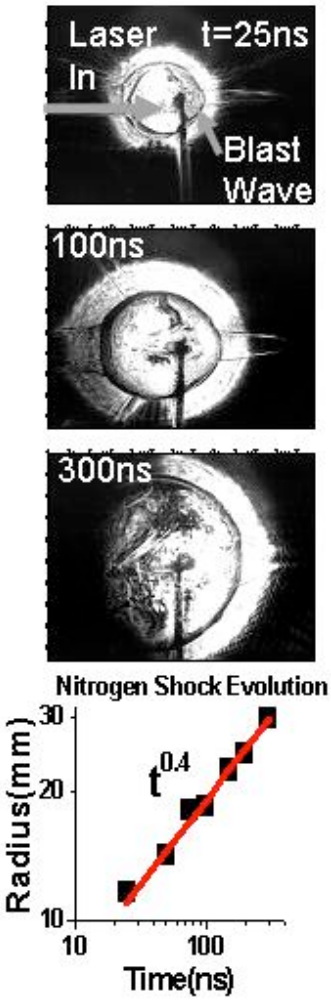

Figure I.A.2: Images of blast waves in nitrogen at 25ns, 100ns and 300ns after a 1000J drive beam has hit a 0.5mm nylon target. Bottom panel is a graph of the radius of the blast waves as a function of time. It shows that the blast waves follow a $t^{0.4}$ trajectory indicating that radiation losses do not play an important role in the hydrodynamics of the blast waves.

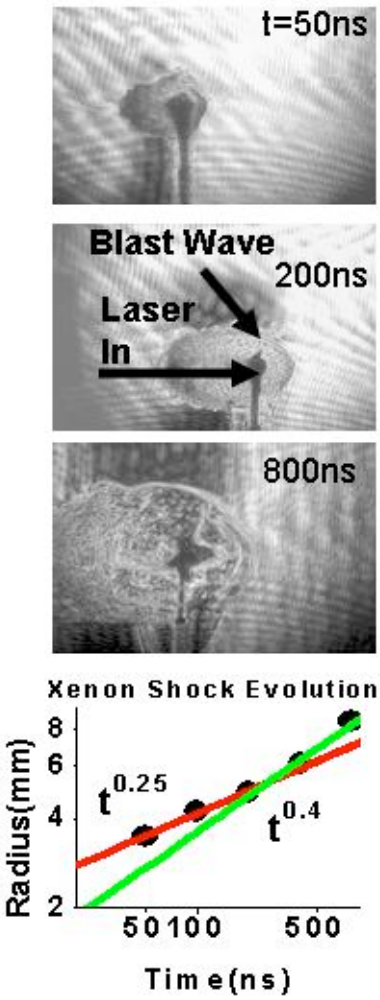

Figure I.A.3: Images of blast waves in xenon at 50ns, 200ns, and 800ns after a 1000J drive beam has hit a 0.5mm nylon target. Bottom panel is a graph of the radius of the blast waves as a function of time. It shows that the blast waves follow a trajectory slower than $t^{0.4}$ before ~400ns, indicating significant energy losses due to radiation.

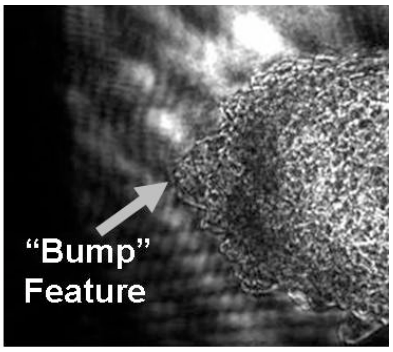

Figure I.A.4: Zoomed in view of bump feature on blast wave 400ns after 1000J laser pulse illuminated a 0.5mm nylon target. Feature is caused by a portion of the blast wave front moving faster in the region heated by the drive laser's passage.

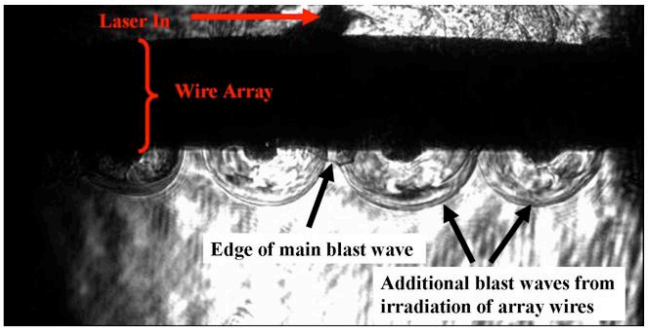

Figure I.A.5: 9mm spaced wire array in xenon gas 700ns after 1000J laser pulse illuminated 0.5mm nylon target. The main blast wave is just passing the wire array. Additional blast waves created by radiation from the main blast wave have already formed around each wire in the array and are moving outward

In order to measure the rate of this decay, we traced out the edge of the blast waves in polar coordinates. We Fourier transformed this curve to select the frequency corresponding to our wire array wave number. An example of the results of this procedure is shown in Figure I.A.7. After we determined the amplitude of the frequency component of interest to us, we plotted this amplitude relative to the radius of the blast wave as a function of time and fit this data with a function of the form $R/A = C*t^p$. We compared these results to theoretical predictions for p as a function of spherical wave number from Vishniac et al. [7]. This comparison is illustrated in Figure I.A.8. Here we see the experimental data compared to theoretical predictions for various adiabatic indices. The best agreement occurs for an effective adiabatic index of 1.4-1.5. This agrees well with our intuition for the nitrogen gas in our experiment. In order to better determine the adiabatic index of our gas, we are currently performing simulations using the Hyades code [18], a 1-D Lagrangian hydrodynamics code with tabular equation of state.

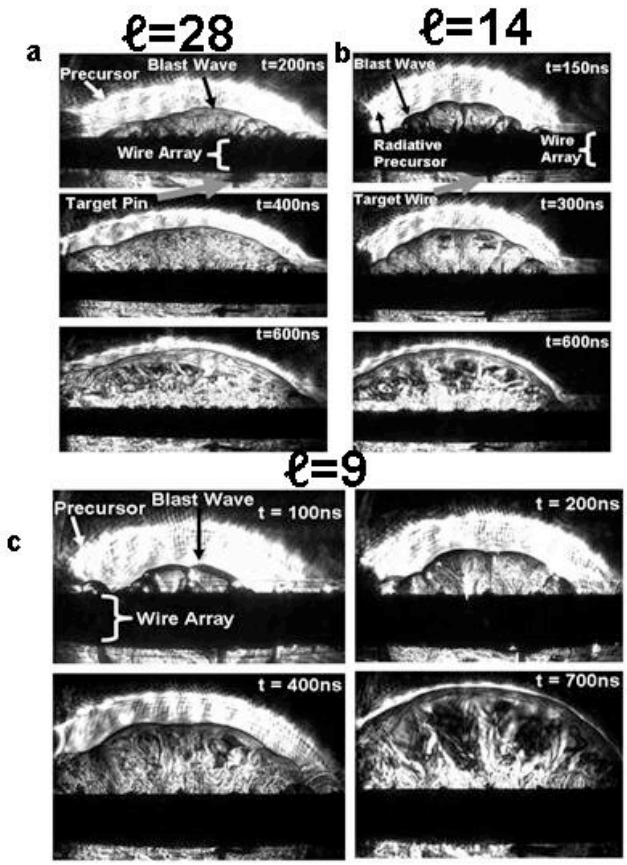

Figure I.A.6: Evolution of perturbations on blast waves produced by a) 2mm, b) 4mm, and c) 6mm spaced wire arrays. The perturbations damp out with time due to the high effective adiabatic index of the nitrogen gas.

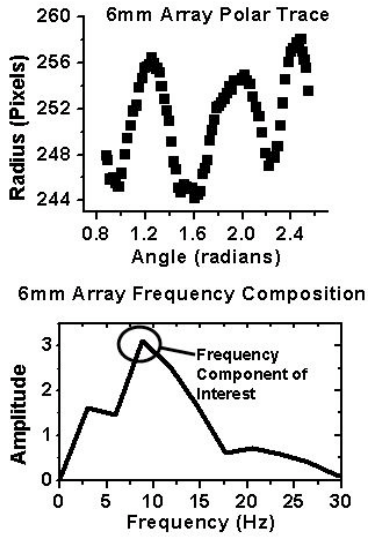

Figure I.A.7: Top panel is the coordinates of the edge of a blast wave moving past a 6mm spaced wire array in polar coordinates. The bottom panel is the Fourier transform of the same shot. Highlighted is a peak at a wave number of ~9, which corresponds to the wave number of the induced perturbation of the wire array.

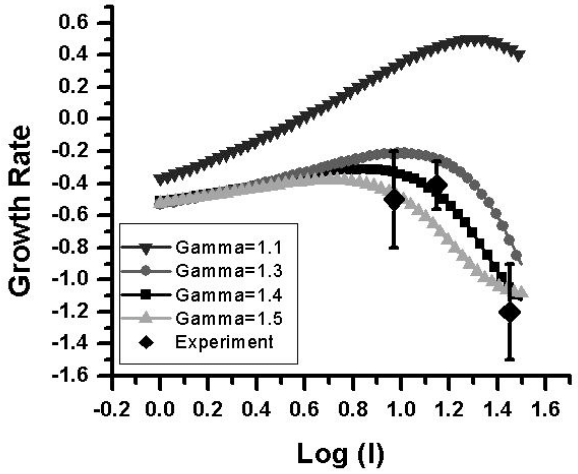

Figure I.A.8: Comparison of experimental results to theoretical predictions for decay rates as a function of wave number of perturbations for blast waves traveling through nitrogen. The experimental results match well to theoretical predictions for a gas with an adiabatic index of 1.4-1.5.

In addition to these studies of blast waves from exploding point like laser plasmas, we have been pursuing a technique to make cylindrical blast waves in a gas jet. This technique will avoid the problem described above in which the laser perturbs the medium as propagates toward the solid target. To do this, we utilize a gas target composed of rare gas clusters. Clusters are an intermediate state between solids and gases and combine efficient energy absorption properties with a low average density. This makes them an ideal medium in which to study highly energetic hydro events.

The experiments were conducted at the University of Texas using the THOR laser system which is a 20 TW-Ti:Sapphire system providing 0.7 J of energy in a 35 fs FWHM pulse at a repetition rate of 10 Hz. The 800 nm wavelength beam was focused to a peak intensity on the order of 10^{19} W/cm_ into a cluster spray. The laser-heated clusters in the focal volume explode, forming a plasma with temperatures of up to 1 keV. Subsequently the plasma explodes hydrodynamically and drives a shock wave into the ambient gas. A 400 nm probe beam maps the expansion process onto a CCD-camera through either an imaging Michelson interferometer or a dark-field schlieren device. The probing pulse is separated from the main beam after the final amplification stage individually compressed in an additional two grating compressor. Its frequency is doubled in a KDP crystal providing 4 mJ of energy in a 42 fs FWHM, 2.5 cm diameter pulse to backlight the plasma filament. The probe beam can arrive there at any time delay Δt with respect to the heating beam within a window of $-3.4ns \le \Delta t \le 97ns$.

Irradiating xenon clusters with the full laser power created radiative blast waves with strong deviations from an adiabatic Sedov-Taylor trajectory. This is shown in figure I.A.9 where the late-time (>10ns) blast wave radius fits to a power law of $\alpha = 0.42 \pm 0.01$. The $\alpha = \frac{1}{2}$ Sedov-Taylor solution is shown in blue. In addition, clear radiative precursors are visible in the dark field schlieren images and in the electron density profiles obtained from the interferograms shown in figure I.A.10.

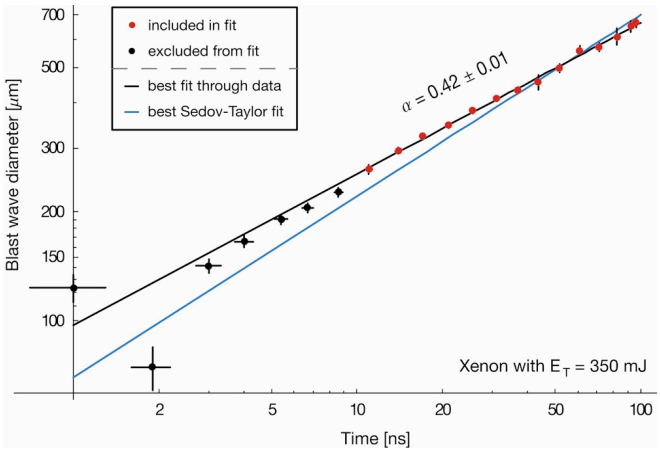

Figure I.A.9. Radiative heat transport in xenon leads to a reduced deceleration parameter [ ].

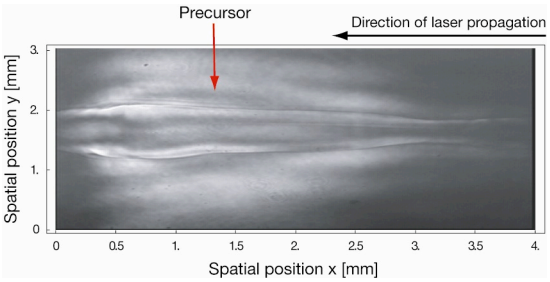

Figure I.A.10. Dark-field images of xenon plasmas show strong evidence of major radiative energy losses.

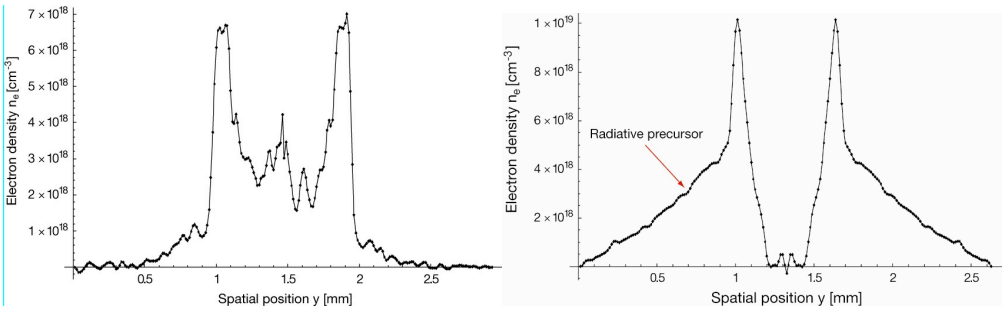

Figure I.A.11 .Electron density profiles in argon (left) and xenon (right). The xenon exhibits a clear ionization precursor ahead of the shock front.

By changing the target gas we can easily change the importance of radiation within the system. The shock fronts in argon drop sharply with very little ionization of the gas ahead of the shock and the blast wave evolution shows no significant deviation from the adiabatic trajectory. As stated before, a radiative loss from the blast wave should increase its compressibility, thinning the shock shell. Indeed, we compared the shell thickness in xenon and argon at equal blast wave radii, shown in figure I.A.11, and found a considerable reduction for the higher *Z* gas.

References for section I.A

1. J. J. Erpenbeck, Physics of Fluids **5** (10), 1181 (1962).
2. P.A. Isenberg, Astrophysical Journal **217** (2), 597 (1977).
3. D. Ryu and E. T. Vishniac, Astrophysical Journal **313** (2), 820 (1987).
4. B. G. Elmegreen and D. M. Elmegreen, Astrophysical Journal **220** (3), 1051 (1978).
5. J. P. Ostriker and C. F. Mckee, Reviews of Modern Physics **60** (1), 1 (1988); G. L. Welter, Astronomy and Astrophysics **105** (2), 237 (1982).
6. E. T. Vishniac, Astrophysical Journal **274** (1), 152 (1983).
7. D. Ryu and E. T. Vishniac, Astrophysical Journal **368** (2), 411 (1991).
8. E. Liang and K. Keilty, Astrophysical Journal **533** (2), 890 (2000).
9. G. Welter and J. Schmidburgk, Astrophysical Journal **245** (3), 927 (1981).
10. J. M. Blondin, E. B. Wright, K. J. Borkowski et al., Astrophysical Journal **500** (1), 342 (1998).
11. M. M. MacLow and M. L. Norman, Astrophysical Journal **407** (1), 207 (1993).
12. T. Ditmire, K. Shigemori, B. A. Remington et al., Astrophysical Journal Supplement Series **127** (2), 299 (2000); K. Shigemori, T. Ditmire, B. A. Remington et al., Astrophysical Journal **533** (2), L159 (2000); M. J. Edwards, A. J. MacKinnon, J. Zweiback et al., Physical Review Letters **8708** (8), art. no. (2001).
13. J. Grun, J. Stamper, C. Manka et al., Physical Review Letters **66** (21), 2738 (1991).
14. J. L. Rambo P. K. Rambo, Jr., G. R. Bennett, I.C. Smith, A.C. Erlandson, J.E. Murray, and J. Caird, OSA Trends in Optics and Photonocs, Conference on Lasers and Electro-Optics **73**, 362 (2002).
15. J.A. Glaze, W.W. Simmons, and W.F. Hagen, *Status of large neodymium glass lasers*. (Soc. Photo-Optical Instrumentation Engrs, Palos Verdes Estates, CA, USA Reston, VA, USA, 1976).
16. Sir Geoffrey Taylor, Proc. Roy. Soc. A **201** (A), 159 (1950); L. Sedov, Prikl. Mat. Mekh. **10** (2), 241 (1946).
17. *CALE Users Manual*. (Lawrence Livermore National Laboratory, 1991).
18. Inc. Cascade Applied Sciences, *HYADES User's Guide*. (Cascade Applied Sciences, Inc., Boulder, Co, 2004).

I.B Shocked materials studies on the THOR laser

Participants:
W. Grigsby, A. Dalton, M. Downer, E. Taleff, S. Bless and T. Ditmire (University of Texas)
Jeff Colvin, and C. Mailhiot (Lawrence Livermore National Laboratory)

A complete understanding of shock waves in materials requires comprehensive microscopic understanding of the compression wave. Within the Center we have undertaken a series of experiments to develop ways of studying atomic scale motions in materials as a material undergoes very high strain rate shock compression.

To study these dynamics we are using short pulse lasers in high time resolution pump-probe experiments. Our initial work is concentrated on examining the shock induced melt transition in Tin.

Ultrafast optical probes can shed light on these dynamics and provides the technique for our initial experiments. The principle behind these experiments is illustrated in figure I.B.1. It is possible to use the fact that the linear and nonlinear optical properties of a material differ when the solid becomes a liquid. This means that the material reflectivity will change as it undergoes a phase transition to a liquid and its nonlinear optical properties can change. The later fact can be exploited if second or third harmonic are generated off the back of a target that is shocked and the harmonic intensity is monitored via pump-probe techniques. This approach has been used in the study of femtosecond laser induced melting in semiconductors such as silicon [1].

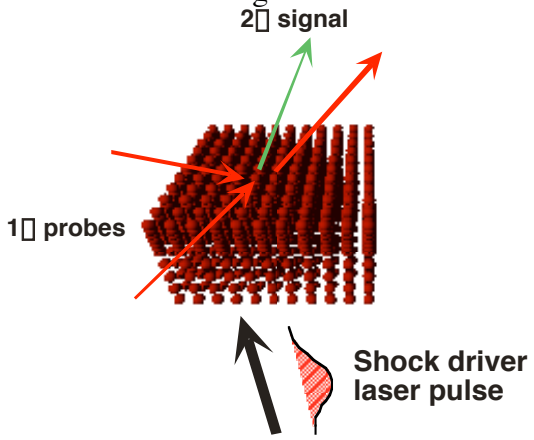

Figure I.B.1: Cartoon of the probing of a shock induced lattice change by optical or nonlinear optical probing.

To illustrate the possibilities in optical time resolved probing of laser produced shocks, we have performed the experiment illustrated in figure I.B.2. We use the University of Texas THOR Ti:sapphire laser. The uncompressed, 600 ps pulse from THOR drives a shock in a thin sample, which is a slab of tin 4 mm thick in our initial proof of principle experiments (chosen to match the shock transit time driven by our 600 ps pulse). This shock is driven by about 1 J of light focused to a 0.4 mm spot. This slab is probed on the back side with part of the laser that has been split from the shock driver laser and compressed to 40 fs time duration. In this way, the ultrafast probe pulse is well synchronized to the shock driver. A CCD camera images the reflection off the back surface of the tin slab. The probe pulse is itself split and sent through an interferometer to derive simultaneous information on the amount of shock driven expansion on every shot. Typical data are shown in figure I.B.3 where the reflectivity of the slab 2 ns after the drive pulse begins irradiating the surface is shown. As can be seen, a well defined region of the tin, where the shock has broken out on the back side, exhibits reduced reflectivity.

A measurement of the reflectivity in the center of the shocked region as a function of time is plotted in figure I.B.4. We observe a quick (<200 ps) drop of the reflectivity to 90% once the shock breaks out from the target surface. A slower, further fall of the reflectivity follows this rapid drop. The dynamics leading to this behavior are still not understood but the early time drop may result from shock melting while the later reflectivity fall may derive from some microscopic

break-up of the surface. The implementation of nonlinear optical probing in the future will help to remove this ambiguity. Future work will benefit from shocking at higher pressure over thicker target slabs using higher energy laser pulses.

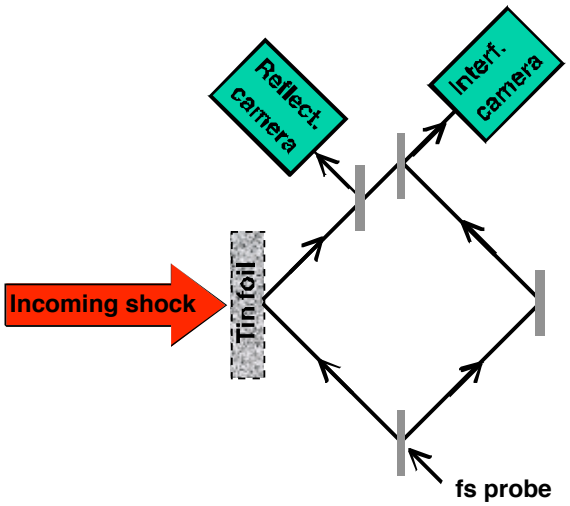

Figure I.B.2: Schematic of the shock induced melting experiment in a tin slab.

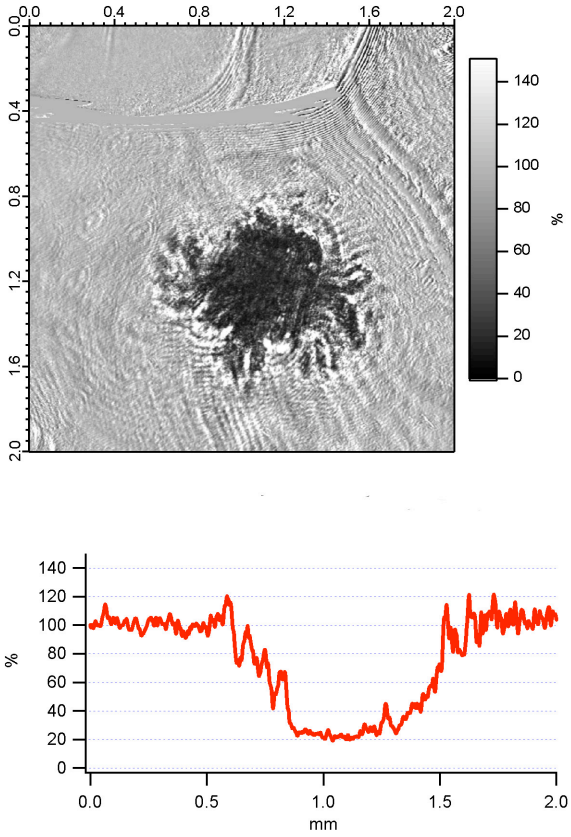

Figure I.B.3: Data showing the drop in reflectivity observed on the back of a tin slab 2 ns after the shock driver laser pulse irradiated the sample.

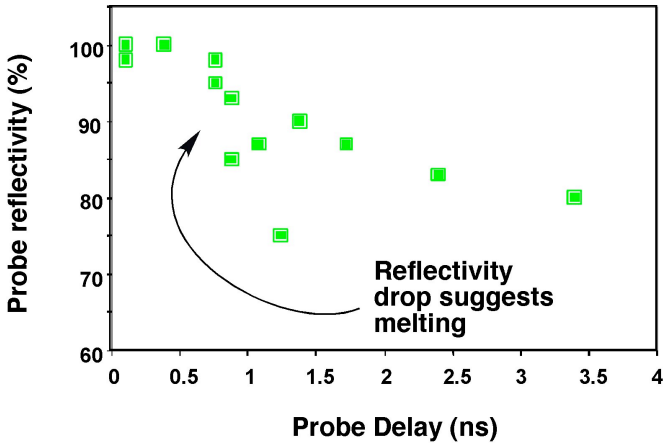

Figure I.B.4: Measured tin reflectivity as a function of time showing the drop in reflectivity coincident with the shock break out.

We can observe the velocity of the release of the target by examining interferometric images of the back surface as a function of time. Figure I.B.5 shows raw 2-D interferometry data on the back of our tine targets. By examining the position of the released material as a function of time, and doing this on a number of targets of different thickness (4-6 μm), we can derive a rough measurement of the tin Hugoniot. These data are shown in figure I.B.6 and are overlaid with previously published, gas gun Hugoniot data for tin. Our points lie on these previously published data though we still must surmount the problem that this technique results in rather sizeable error bars.

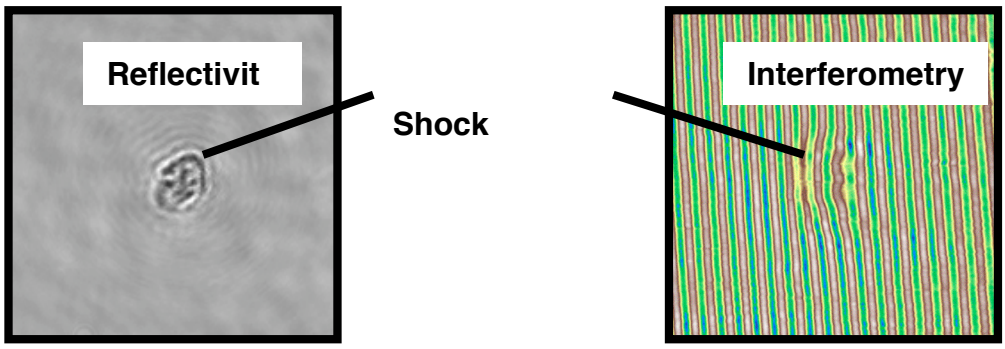

Figure I.B.5: Images pf reflectivity and interferometry diagnostic on 4 μm tin slab 1 ns after the shock has arrived at the back surface.

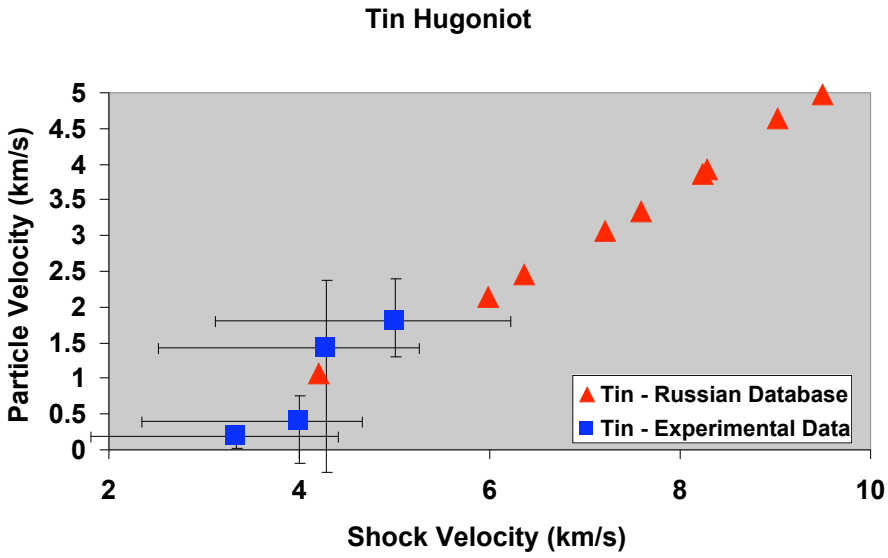

Figure I.B.6: Measured tin Hugoniot data overlaid on gas gun data from ref. [2].

References for section I.B

1. Shank, C. V., Yen, R. and Hirlimann, C. *Phys. Rev. Lett.,* **51**, 900 (1983).
2. Data taken from: http://teos.ficp.ac.ru/rusbank/

I.C Molecular Dynamics simulations of high strain rate shocks

Participants:
M. Lane and M. Marder (University of Texas)

In support of our tin shock experiments, we have also undertaken a simulation study of shocks in tin. We use molecular dynamics (MD) techniques developed at UT Austin in the Center for Nonlinear Dynamics.

MD simulation of shockwaves in model systems was established in the early 80's and ever-larger computations are bound only by the computing power of the day. MD study of shocks requires large computational facilities, since long-time shock simulations require large amounts of material to be simulated. The problem does not easily allow for small systems to run for long times, or large systems to run for short times. Success in the field has been found by pushing forward with multi-million atom simulations on the nation's largest parallel machines.

Our simulation focus has been on the shock front, a relatively small neighborhood at the interface between compressed and uncompressed material. Our interest is in the transitions at this front, and how they depend on the forcing parameter for the shock wave. Our studies are demonstratingthat we can simulate conditions at the front without the large system sizes usually

necessary to study long-time shock propagation.

We employ a moving window technique in which only a small portion of the physical system is simulated. To accomplish this, we are constantly feeding fresh material to the system, and purging compressed material from behind the shock. The concept of a moving analytical window for studying shockwaves was first proposed by Klimenko and Dremin [1] as a means to time average fluctuations in a small system. Zhakhovskii, et al. [2] later improved on this method, but relied on - without fully describing - a ``special potential'' which functioned as a permeable piston at the back surface. Our purge criterion and purge method are based on firm principles of shock theory and statistical mechanics. The basic idea is to ensure that material behind the shock front has sufficiently approached thermodynamic equilibrium in the moving frame. So long as this condition obtains, discarding material should have little effect upon shock dynamics.

Crystal far enough ahead of the shock front is unperturbed by it, because shocks travel faster than any wave in the uncompressed material, and because our interatomic potential is short-ranged. Thus, neither direct particle interaction nor wave interaction can influence particles more than 10 Angstrom ahead of the front, We limit our simulation size by adding particles only as they come within a buffer zone >50 angstrom from the shock front. We add complete unit cells when we paste particles onto the front of the sample, and the front edge of the simulation is constrained to prevent unphysical surface reconstruction.

The code [3] used for this work is developed and maintained at the University of Texas at Austin. It has been applied to nonequilibrium problems in fracture, friction and shock simulation. The code is spatially parallel for scalability. We use classical molecular dynamics with an effective interatomic potential. The equations of motion are integrated by the Verlet method with a timestep of 0.3 femtoseconds. Temperature is monitored but not externally controlled. Shock waves are generated by moving an infinitely massive piston (momentum mirror) at a constant velocity into an initially stationary material. The piston velocity is the independent variable. In all of our runs, the tin crystal is oriented so that the shock runs along the [100] direction.

The Modified Embedded Atom Method (MEAM) of Daw and Baskes is used to model the atomic interactions. We employMEAM parameters due to Ravelo, et al. [4] which were determined by fitting structural, transitional and melt properties with experimental values to within 11%. Our simulations vary in size, with a minimum cross section of 5x5 units cells. Periodic boundary conditions are imposed in the directions transverse to shock motion. Particle numbers in our preliminary runs have been small, ranging from thousands to tens of thousands. In all cases simulations run until transients die away, requiring more than 10,000 timesteps in every case.

As a compressive shock wave propagates, it converts pristine material ahead into denser material behind. Long shock simulations require large amounts of material to be simulated, although the shock front constitutes only a small part of the entire system. Our moving window technique simulates only the particles in the neighborhood of the moving front by adding material ahead of the shock only as needed, while purging from behind the shock when derived physical criteria

are met.

The shock front is undisturbed by crystal ahead of it, and the crystal far enough ahead is unperturbed by the shock front. These statements hold because shocks travel faster than any wave in the uncompressed material, and because our interatomic potential is short-ranged. Thus, neither direct particle interaction nor wave interaction can influence particles more than 10 Angstrom ahead of the front, We limit our simulation size by adding particles only as they come within a buffer zone >50 angstrom from the shock front. Particles are added as complete unit cells, and the front edge of the simulation is constrained to prevent unphysical surface restructuring.

We contend that under many conditions particles behind the shock front can also be removed from the simulation. Here, there is no argument that waves cannot influence the front, since shocks are always subsonic in the compressed material. So, we must limit ourselves to steady state fronts. In these cases, we have developed a simple criterion for when material at the back edge can be purged.

Consider a material through which a perfect one-dimensional shock front is propagating. Take the shock as an abrupt change in ρ the density, and u the particle velocity. If a right-traveling disturbance moves with speed U, then one can balance the mass entering the region of abrupt change (the shock front) from the right with the mass leaving the region on the left.

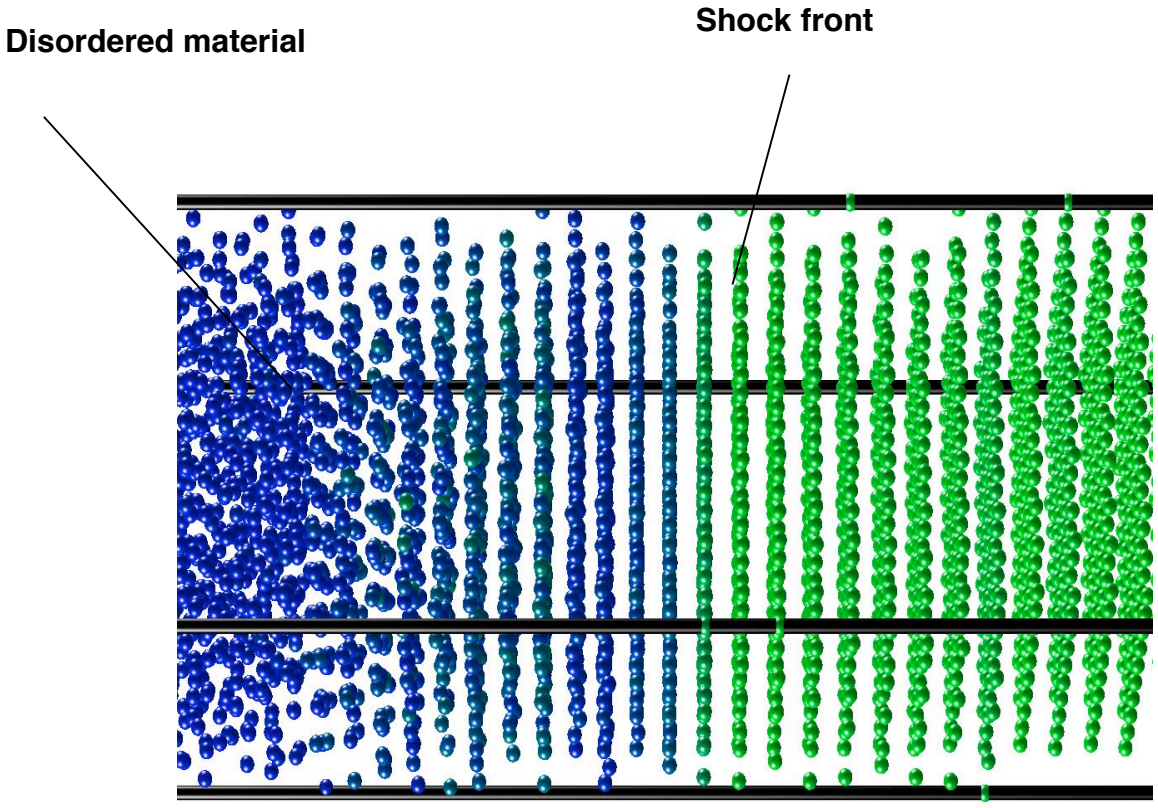

Figure I.C.1: Image of a simulated shock in a tin lattice. Color of the particle denotes the energy.

In a given time Δt, the mass entering the region on the right is given by the product of the density and the volume flux into the region. The volume flux is given by the product of A the cross sectional area the relative velocity of the shock front, u_0-U, and Δt the time interval. Using the well known jump conditions [4] for a shock front we can form a simple physically meaningful criteria for purging material from the back surface. Thus, as the shock front propagates through our system, it's position is periodically calculated. This position is first compared to the front

boundary of the system. If the shock front has entered the buffer zone, then a unit cell thickness of particles are added to the system ahead of the shock front. At each of these add events, the system's back boundary is also evaluated for a purge. If the average conditions within a volume equal to the volume just added satisfy the purge criterion, this volume is removed from the system and the porous piston is advanced. Such that, if an add and purge event occur simultaneously then the total system volume would remain constant and the number of particles in the system would decrease.

We have performed preliminary simulations on tin. One result is illustrated in figure I.C.1. We find that our simulations agree well with published Hugoniot data on tin, validating the potentials used in our simulations. A comparison of the Hugoniot derived in our MD simulations is compared to tine Hugoniot data in figure I.C.2

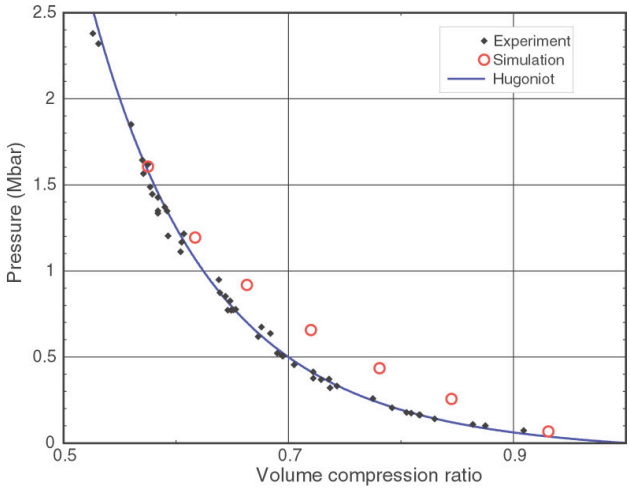

Figure I.C.2 Comparison of simulated tin Hugoniot points with data points

References for section I.C

1. V. Yu. Klimenko and A.N. Dremin. Soviet Physics Doklady, **25(4)**:288--289, (1980).
2. V. V. Zhakhovskii, S. V. Zybin, K. Nishihara and S. I. Anisimov, Phys. Rev. Lett. **83,** 1175 (1999).
3. B.L. Holian, et al., and R.~Ravelo, M.D. Furnish et.al., editorShock Compression of Condensed Matter - 1999, pages 35--41. AIP Conference Proceedings, 1999.
4. Y. B. Zel'dovich and Y. P. Raizer, *Physics of Shock Waves and High-Temperature Hydrodynamic Phenomena*, (Academic Press: 1967).

I.D Neutron generation studies

Participants:
K. Madison, D. Symes, R. Hartke, F. Buergens, R. Bengtson and T. Ditmire (University of Texas)
P. Patel, and D. Price (Lawrence Livermore National Laboratory)

Within TCHILS we have an ongoing interest in the production of intense bursts of neutrons by short pulse laser driven deuterium fusion. Ultimately, we hope to field these kinds of experiments on the Texas Petawatt laser with the intent of producing enough neutrons to perform time resolved materials damage studies with the short pulse of neutrons acting as a pump. Consequently, we have put effort into understanding the yield scaling of neutrons with an eye toward ascertaining the scaling toward a petawatt. Much of the core of this work has been performed in recent years in collaboration with people from LLNL. We are now beginning to collaborate with simulation experts at Sandia as well on this project. Work within the Center during the last year has been an extension of our ongoing work in this area over the past few years.

The approach that we have been studying relies on the fact that very high ion temperature plasmas can be produced when an intense, femtosecond pulse irradiates a gas of van der Waals bonded clusters. When a gas of deuterium clusters is used as a target a plasma of sufficiently fast deuterium ions can be produced to drive DD nuclear fusion. The idea of these experiments is illustrated in figure I.D.1. A high intensity, ultrafast laser pulse is focused into a gas jet of deuterium clusters, creating a plasma filament with a diameter roughly that of the laser focus (~100 μm) and a length comparable to the extent of the gas jet plume (~ 2 - 5 mm). The fast deuterium ions ejected from the exploding clusters can then collide with ions ejected from other clusters in the plasma driving DD fusion and releasing neutrons from one branch of the fusion reaction, $D + D \rightarrow He^3 + n$, in which a neutron is released with 2.45 MeV of energy.

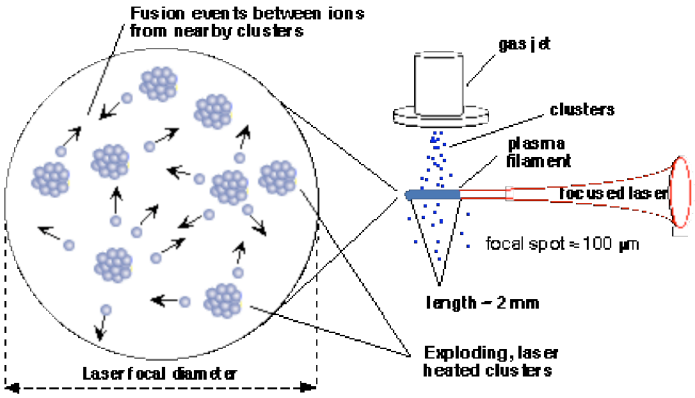

Figure I.D.1: Schematic of the deuterium cluster fusion experiment.

This fusion was first observed in cluster deuterium plasmas in initial experiments at LLNL where we observed up to ~ 10^4 DD fusion neutrons at 2.45 MeV per laser shot with roughly 100 mJ of laser energy focused to intensity of 10^{17} W/cm^2 [1]. The yield scaling with laser energy in these experiments is shown in figure 5 (labeled "Falcon data"). Recently, the group at LOA in France

have also observed fusion from the Coulomb explosion of deuterated clusters and have observed fusion yields which are consistent with our initial experiments [26]. Since the initial experiments reported in [2], we have characterized the scaling of the fusion yield to higher laser energy. To do this, we used the LLNL JanUSP laser which delivered up to 10 J of energy in 100 fs pulses [3]. Data on the neutron yield from the irradiated cluster plume were acquired with an array of plastic scintillating detectors as a function of pulse energy for 100 fs and 1 ps pulse durations, results which are also shown in figure I.D.2. We find that the fusion yield increases rapidly with laser energy, increasing roughly as the square of the energy for all pulse durations [4]. During the past year, under support from the Center we can repeated these scaling experiments on the UT THOR laser. These data are also illustrated in figure I.D.2.

The fusion yield scaling in these experiments can be estimated by noting that the expected fusion neutron yield for the cluster gas jet experiment will be approximately: $N \propto \langle \sigma_{DD\,nHe} v \rangle n_i^2 \tau_{dis} V$ where n_i is the D^+ ion density (>2 x 10^{19} cm^{-3} in cooled jets), τ_{dis} is the disassembly time of the plasma, $\langle \sigma_{DD\,nHe} v \rangle$ is the velocity averaged fusion cross section (for the D+D $\rightarrow$ He^3 +n reaction) and V is the plasma volume. The yield is directly related to the disassembly time of the plasma, which is, for the inertially confined plasmas of the experiments described above, roughly the time required for a deuteron to exit the plasma by free streaming across the filament diameter. Our observed fusion yield in all cases is consistent with equation above (where $\langle \sigma v \rangle \sim 10^{-19}$ cm^3 s, $n_i \sim 10^{19}$ cm^{-3}, $\tau \sim$100 ps and $V \sim$0.03 mm^3 for 100 mJ shots implying a yield, N ~ 3 x 10^4 /shot). A large gain in yield could be derived if τ_{dis} could be increased.

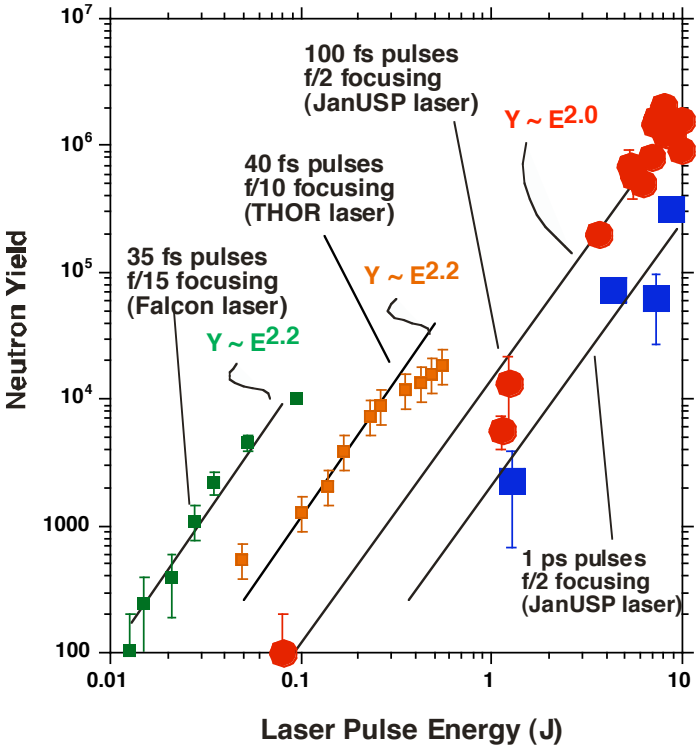

Figure I.D.2: Measured scaling of cluster fusion yield as a function of laser energy. These data were acquired with three different laser systems.

During this the past year, we started studies of exploding mixed species CH_4 and CD_4 clusters. Heteronuclear clusters like deuterated methane are very interesting since these mixed ion clusters may exhibit enhancements in ion energy through a dynamical effect in the Coulomb explosion. The Coulomb explosion of a single species cluster, like D_2 clusters, will eject deuterons with an energy given directly by the potential energy of the ion as it is initially in the fully stripped cluster. In exploding mixed ion clusters like CD_4 the light deuterons will outrun the heavier ions, explode in an outer shell with a higher average energy than would be expected from the naïve estimate of ion energy based on initial potential energy. This implies that the fusion yield could be substantially increased in plasmas formed from explosions of heteronclear clusters over that of neat D_2 clusters of the same size because of this kinematic enhancement of ion energies in the mixed ion case. We examined the explosion of CD_4 clusters and the fusion yield that results from these plasmas. Those experiments indicated that there was some enhancement of deuteron energies from CD_4 when compared to similar sized D_2 clusters.

This year, we followed up on these experiments motivated by a surprising result published recently by the LOA group in France [5]. This group reported what seemed to be a rather large (>40%) anisotropy in the neutron emission from exploding CD_4 cluster plasmas. This is unexpected if the pure Coulomb explosion model is at work since the clusters should eject ions nearly isotropically. We examined the angular distributions from these clusters using the apparatus illustrated in figure I.D.2. Here we examined the distributions of neutrons as a function of polarization angle in the laser polarization plan as well as a function of azimuthal angle in the plane of propagation. The French group reported a large peaking of the neutrons perpendicular to the laser propagation direction.

Our results are quite at odds with the French results. We find, first that there is nearly completely uniform neutron emission with polarization angle. We do observe a slight anisotropy in the azimuthal plane. This is illustrated with the data shown in figure I.D.4. Here the neutron emission from a CD_4 cluster plasma, irradiated with 0.5 J of a 40 fs laser pulse is shown. The cluster sizes are around 10 nm per cluster. We see a small peaking of the neutron emission in the forward and backward direction (ie along and and back against the laser propagation axis). This anisotropy is much smaller than reported by the LOA group and is in a direction different than they see. We believe that our result is, in fact, completely in keeping with the Coulomb explosion picture of the cluster explosion, and that the slight neutron peaking can be explained by the cigar shaped plasma filament geometry of the plasma. A detailed explanation of these results as explained by detailed Monte Carlo particle simulations will be presented in a paper currently under preparation.

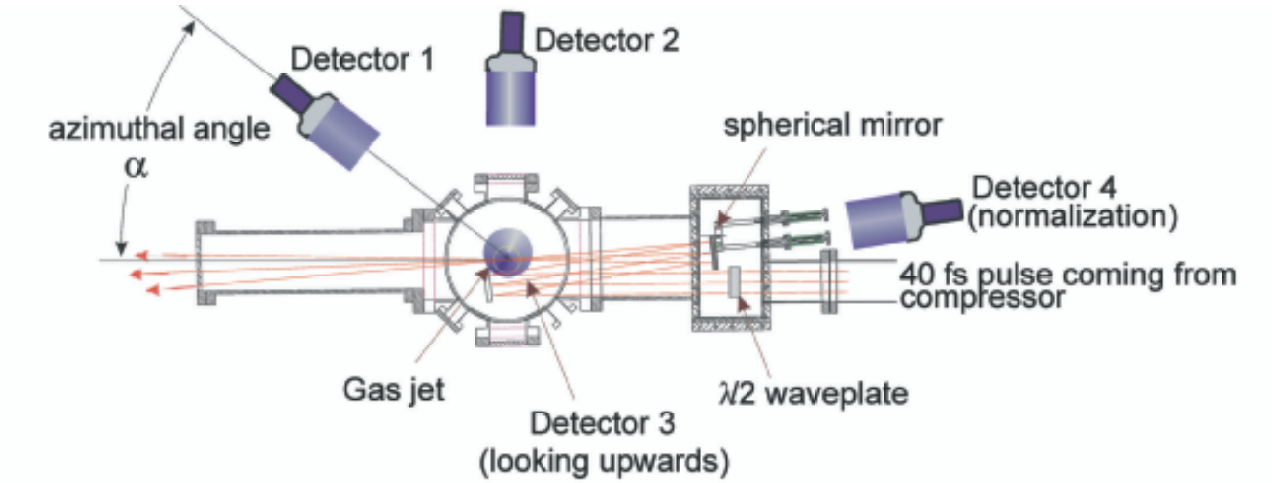

Figure I.D.3: Experimental set-up used for measuring the neutron angular distribution on the UT THOR laser.

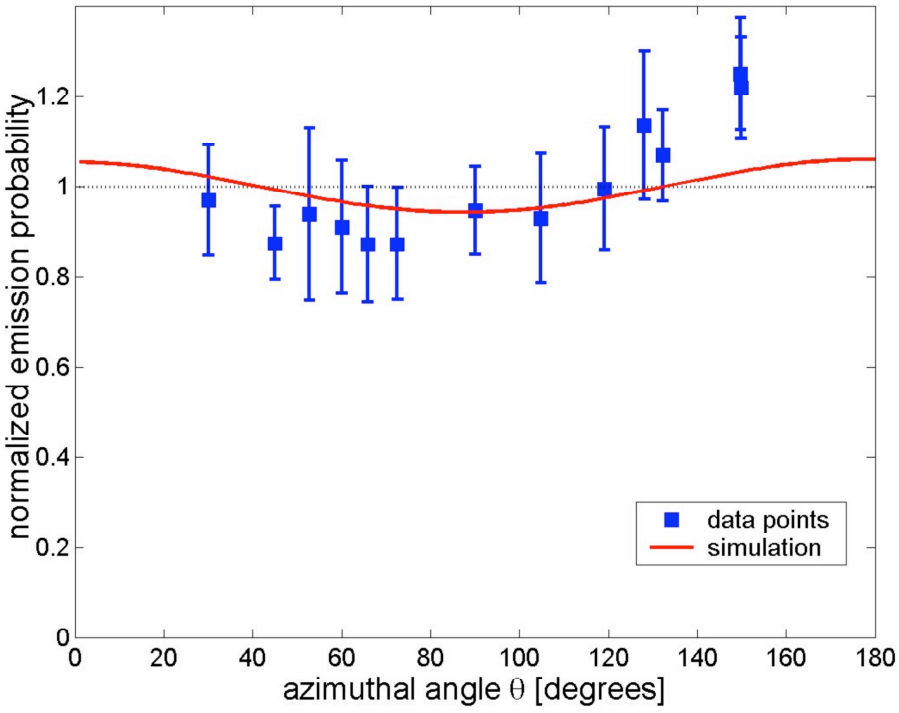

Figure I.D.4: Azimuthal scan of neutron yield from CD_4 clusters carried out by an angular scan of 'Detector 1' shown in Figure I.D.3.

References for section I.D

1. T. Ditmire, *et al.*, , *Nature* **398**, 489 (1999).
2. J. Zweiback, *et al.*, , *Phys. Rev. Lett.* **84**, 2634 (2000).
3. J. D. Bonlie, F. Patterson, D. Price, B. White, and P. Springer, *Appl. Phys. B-Lasers Opt.* **70**, S155 (2000).

4. K. W. Madison, R. Fitzpatrick, P. K. Patel, D. Price, T. Ditmire, *Phys. Rev. A*
5. G. Grillon*, et al.*, *Phys. Rev. Lett.* 89, art. no.-065005 (2002).

I.E K-alpha x-ray production studies at the UT THOR laser and the LLNL COMET laser

Participants:
G. Dyer, B. Cho, D. Symes, and T. Ditmire (University of Texas)
S. Gaillard, Y. Sentoku, T. Ohkubo, N. LeGaulladec and T.E. Cowan (University of Nevada, Reno)
R. Shepherd, H. Chen, K. Widmann (Lawrence Livermore National Laboratory)

Within TCHILS we have an interest in developing bright K-alpha x-ray sources. The motivations for doing this include a desire to produce x-rays with enough intensity to heat a secondary target for warm dense matter studies and desire to produce a bright x-ray backlighter source. Both motivations will ultimately see utilization on the Texas Petawatt laser and, perhaps, Z-Petawatt at Sandia. We also have a new interest in proton production (explained in more detail below) for similar applications.

K-alpha x-rays and proton beams can be readily produced with a multi-terawatt laser focused onto a simple thin foil. In this case, the source size is quite small (<1mm), but can be considerably larger than the laser focal spot size [1]. Where greater concentration of the source is desired, alternate target geometry may be capable of guiding absorbed energy in the form of hot electrons interacting with the electromagnetic fields of the laser into a smaller volume, improving concentration and intensity. This is the concept behind using conical targets, which are studied for their application to fast ignition [2]. Utilizing target geometry in this way holds the possibility of generating a source that is superior for many applications.

Since cone targets are difficult to produce and expensive to buy, our study this year focused on an analogous but much simpler to produce target geometry: The pyramidal, or square-based cone geometry. In the experiments reported here, these pyramid targets are irradiated with the 15 TW THOR laser and the x-ray, electron and proton source characteristics are studied with a variety of diagnostics. Our experiments were performed on the THOR laser using up to 600mJ of 800nm laser light on target in a 38fs laser pulse that was focused to a spot of less than 10μm in diameter, yielding intensities of over 10^{19}W/cm^2 available on demand. Diagnostics included proton and electron spectrometers, x-ray pinhole cameras, a Faraday cup, and a six-channel hard x-ray spectrometer. Additional diagnostics scheduled for fielding in early 2005 include a spherical crystal x-ray spectrometer and a low-noise x-ray camera for photon counting.

Pyramidal targets are etched from Si wafers using standard lithographic techniques. We use a high-precision photomask to create a Si_2N_3 mask on the wafer's surface, which is then anisotropically wet etched. The resulting pyramid walls are 111 crystal planes of the Si crystal, meeting at a point which is sharper than 1μm x 1μm (see figure I.E.1). In standard configuration, the polarized laser light has an electric field component that is directed into the plane of two opposing sides of the pyramid.

PIC simulations suggest that free wave electron acceleration and magnetic field guiding of hot electrons will occur in these tapering targets [2]. Hot electrons generated and guided in this waycontinue past the pyramid tip and should continue through any material beyond with the improved localization imposed by the target geometry [1]. In order to select the energy of Ka photons produced a thin foil of some other material is affixed to the back side of the silicon wafer, which is less than 10μm behind the pyramid tip. Using a material of higher Z than Si, the Ka x-rays produced from these hot electrons can be easily distinguished from those produced within the Si wafer.

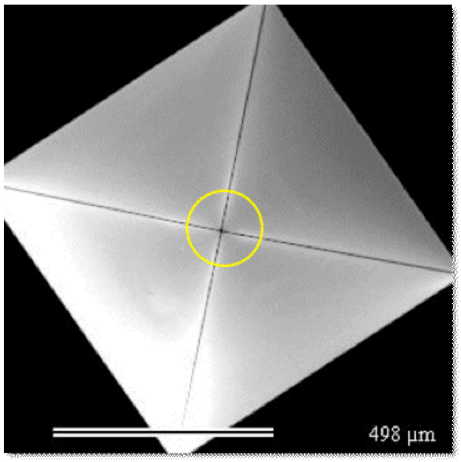

Figure I.E.1 SEM image of pyramid target. The pyramid is etched into a silicon wafer, with the pyramid tip being the deepest point. The tip is less than 10µm from the back surface of the silicon wafer.

Pinhole cameras were used to image x-ray emission from flat, 15μm thick titanium foils as compared to emission from pyramid targets backed with these same foils. Filtering for the pinhole cameras were set to reject the Ka of silicon while passing the Ka of titanium. The foils were shot at a laser incidence of 45°, with P-polarization whereas pyramid targets were shot along the pyramid axis of symmetry (see figure I.E.2).

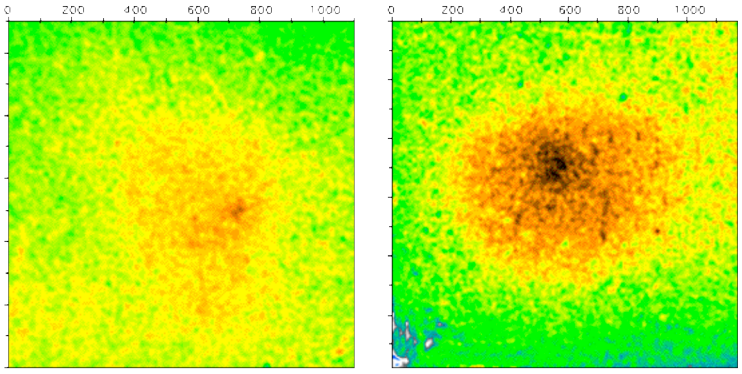

Figure I.E.2 Pinole images of x-ray emission from 25µm Ti foil (left) and pyramid targets with the same foil adhered to their back surface. Filtering on the pinhole camera excludes x-rays below 2.5keV in energy.

These early data are quite promising because they show both an enhancement in overall signal as well as a sharper peak in the region of x-ray emission for the pyramid targets as compared to

plain flat targets. As mentioned above, proton and electron spectrometers are being fielded with these targets, and use of an x-ray spectrometer centered at the titanium K-alpha wavelength is slated for early 2005. Through a photon-counting CCD setup, an absolute comparison of K-alpha output from flat foils and foil-backed pyramid targets. It may be noted that these pyramids are pits in bulk silicon, rather than hollow free-standing pyramids, which would be more analogous to the cone targets studied for fast ignition. Although the tip of our pyramid targets are within less than 10μm of the wafer's back wall, the rest of the pyramid is surrounded by bulk Si. As this may not always be desirable, work is underway to use the silicon pyramids as a mold for creating thin-walled gold pyramid foils, created by vapor deposition followed by etching away of the silicon. In collaboration with UNR we have conducted a preliminary shot series on these free standing gold pyramids though results are still under analysis.

In addition to these cone experiments on THOR, we have been involved in a collaboration performing experiments at LLNL. We participated in an experiment on the COMET laser at LLNL which delivers 1-3 joule, 500 fs pulses onto a solid target. In these experiments, we examined the time history of the K-alpha emission from tin and the He-alpha emission from hot Al. The targets consited of a thin Al overlay deposited onto a tin slab. We used an ultrafast x-ray streak camera to observe simultaneously the time history of emission of the Ti K-alpha and Al He-alpha in these layered flat-foil target. Streak camera data from these experiments is illustrated in figure I.E.3. The Ti K-alpha emission is just to the left of the Al He-alpha emission in this figure. The data indicate that K-alpha emission had a duration of several picoseconds, with the He-alpha, which arises not from hot electrons but from the hot, thermal plasma at the target surface, lasting for several tens of picoseconds. An imaging crystal spectrometer indicated that the K-alpha source size was on the order of 100μm.

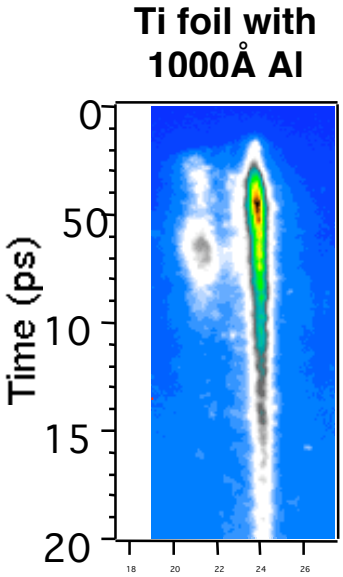

Figure I.E.3: Stream camera image of emission from Ti K-alpha (left trace) and Al He-alpha (right trace). Time axis is vertical.

References for section I.E

1. R. B. Stephens, et al. Phys. Rev. E. **69**, 066414 (2004)
2. Y. Sentoku, H. Ruhl, Y. Toyama, R. Kodama, T. E. Cowan, Phys. Plas **11**, 6 (2004)

I.F X-ray generation from sphere targets

Participants:
D. R. Symes, H. A. Sumeruk, I. V. Churina, J. Landry and T. Ditmire (University of Texas)
T. D. Donnelly (Harvey Mudd College)

In addition to exploring the use of cone targets for x-ray production, we are exploring other, unique targets for x-ray production. In particular, we have begun a campaign in the Center to study hot electron generation and x-ray production from targets coated with microspheres. This work is motivated by the possibility that spheres with size comparable to the wavelength of the incident laser radiation can result in electric field enhancements through well know Mie resonances. This local field enhancement could then lead to more efficient electron generation and brighter x-ray production. The idea of using micro structured targets for x-ray p[roduciton with an intense laser is not new. Recent experiments have demonstrated enhancements in x-ray yield achieved by using structured surfaces such as gratings [1], velvets [2], and nanoparticles [3]. The use of well defined, monodisperse microspheres offers the advantage of exploiting the Mie resonance in a controlled way.

This past year we investigated hard x-ray (>100 keV) generation from copper targets coated with a partially covering layer of microspheres. When a spherical object is illuminated with light of a wavelength,, similar to the diameter, *d*, of the object, a complicated electric field pattern arises due to interference between the incident and scattered waves. The interaction of an intense laser with such a target can generate a spherical plasma with non-uniform heating across its surface [4, 5]. For example, figure I.F.1 displays the electric field pattern of a 1□m spherical plasma irradiated with 0.8 □m laser ligh t. In particular, when the size parameter $m = \pi d/\lambda \sim 1$, the system can experience a Mie resonance in which the electric fields are greatly enhanced. By depositing wavelength-length scale spheres across the surface of a metal substrate, we aim to exploit the Mie resonance to increase the temperature of the resonantly heated electrons which are responsible for the generation of hard x-rays.

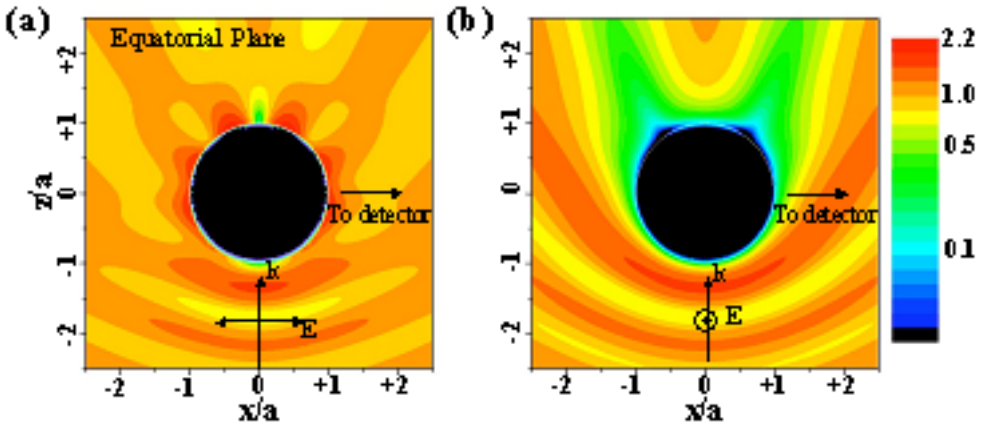

Fig. I.F.1. Calculated electric field plot for an ionized, micron-diameter plasma sphere for laser polarization (a) parallel and (b) perpendicular to the page. The laser propagation direction is +z. Note the enhancement in the field visible in (a). The strength of the electric field is color coded as a ratio of the field strength in vacuum. A field enhancement of over x2 at the sphere's surface is observed in the simulation.

We prepared the targets using commercially available polystyrene spheres of diameter 0.26, 0.5, 1.0, 1.5 and 2.9 μm with a size distribution of 3%, diluted with water to a concentration of ~1:1000, and applied to polished copper substrates. The solution was made more dilute for the smaller spheres to improve the consistency of the surface. We observed the target surfaces using a scanning electron microscope (SEM) to ascertain the uniformity of the coating and to check the depth of the sphere layers. SEM images of copper coated with a 2.9 μm sphere solution, shown in figure I.F.2, at magnification of (a) 100x and (b) 5000x demonstrate that the spheres form a monolayer over a large area.

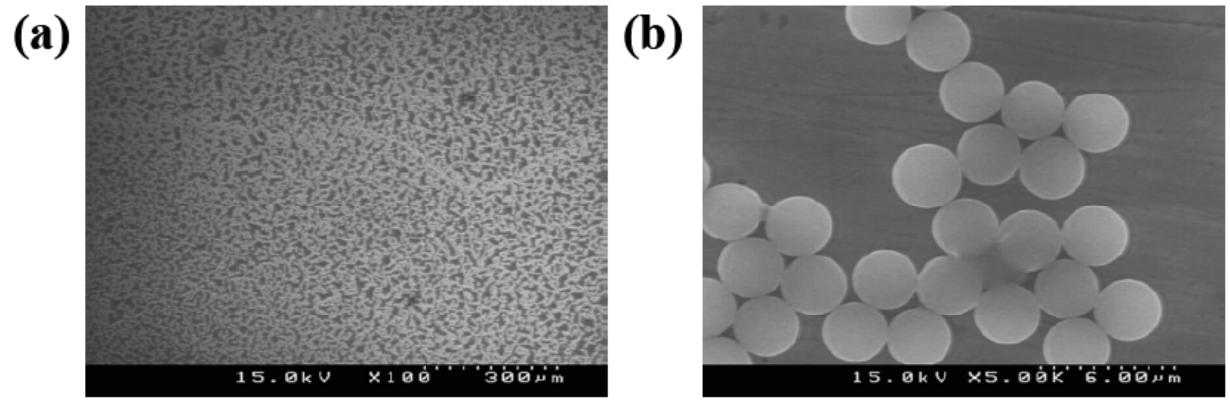

Fig. I.F.2. Scanning electron microscope images of a copper substrate coated with 2.9 μm spheres at (a) 100x and (b) 5000x magnification. Note the uniformity of coverage in (a) and the size consistency shown in (a).

We performed the experiment using the THOR laser system. The pre-compression energy was set at ~68 mJ yielding a focal intensity ~$1x10^{18}$ Wcm^{-2}. This limit was required to avoid saturation of the x-ray detectors. X-ray emission from the plasma was observed using six filtered NaI scintillation detectors arranged around the target chamber. The filters were composed of 125 mm Al (450 keV), 12 mm Cu (162 keV), 32 mm Cu (500 keV), 43 mm Cu (600 keV), 24 mm Pb (700 keV) and 44 mm Pb (900 keV), where the bracketed values are the $1/e^2$ cutoff energies of each filter after accounting for any extra material between the detector and the target. Ion emission from the front surface of the target was measured using a charge collector (Faraday cup) at a distance of 0.20 m behind a mesh biased at -300V to reduce the emission of secondary electrons from the detector surface. A magnetic field of 1 kG was placed ~1 cm in front of the collector to deflect electrons.

We irradiated polished copper targets at laser incidence angles between 0° and 45° from the target normal to ascertain the optimum angle for hard x-ray production under our conditions. The maximum x-ray emission occurred for an incident angles ~10°-20° suggesting that the dominant mechanism for hot electron generation was resonance absorption. The signal levels reduced towards 45° indicating that vacuum heating was inefficient. This was probably due to the formation of a preplasma caused by the interaction of a low level prepulse.

X-ray yields and ion spectra from polished copper targets were then directly compared to sphere coated copper targets at incidence angles of 0°, 10°, 24° and 45°. Initial results using 2.9 μm spheres are shown in Figure I.F.3 and I.F.4. Figure I.F.3 shows the x-ray yield through the 32

mm Cu filter corresponding to an integrated signal of photon energies above ~500 keV. The sphere-coated targets display a clear enhancement in yield at all four angles of incidence of the laser beam, even where resonance absorption is expected to be optimized in the polished copper target. This suggests that the presence of the spheres not only modifies the target surface allowing resonant processes at off-resonant angles but also increases the magnitude of the driving fields through an interference effect (Mie resonance) as predicted. We note that the size parameter for these spheres is relatively large, m=11, so the effect for smaller spheres should be even more significant.

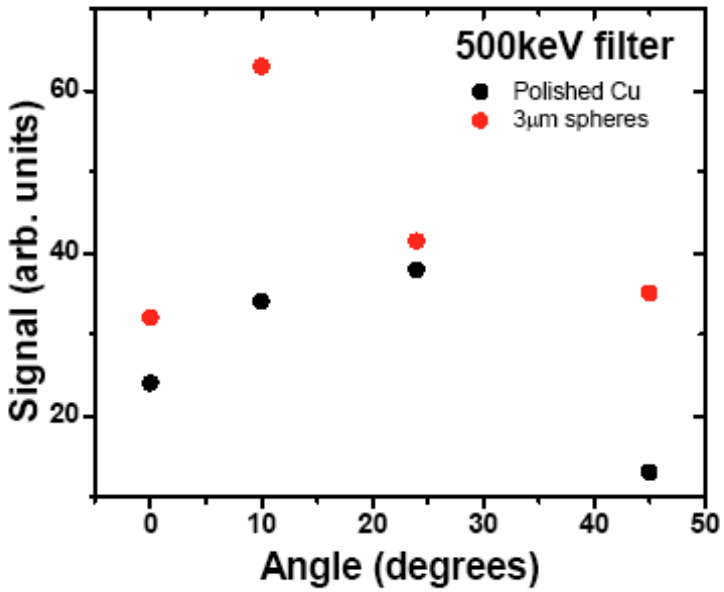

Figure I.F.3. Hard x-ray yields versus angle of incidence of the laser beam for polished copper targets and 2.9 _m sphere coated copper targets.

Time-of-flight (TOF) traces from polished copper and 2.9 μm sphere-coated copper, shown in figure I.F.4, for an incident angle of 45° differed considerably. The earliest time we could resolve after the photon and hot electron burst was ~1.12 ns. This TOF corresponds to protons of energy ~200 eV, below which protons would be deflected by the 1 kG magnetic field. The maximum visible energy of ~10 keV (assuming the ion mass of copper) is too low considering the much higher electron energies implied by the x-ray measurements. This suggests that we only see the colder ions from a distribution driven by two electron temperatures [6]. It is likely that the TOF trace from the sphere targets is predominantly carbon and oxygen whereas the signal from the metal may contain all three species (since contaminants will be present [7]). However, when we irradiated copper coated with a thin plastic film (13 μm), no ion signal was visible implying that the entire trace shown is due to copper ions. This would imply a significant shift in the thermal temperature of the plasma between the two cases and an energy spectrum calculated assuming that all the signal comes from copper ions is shown in the inset.

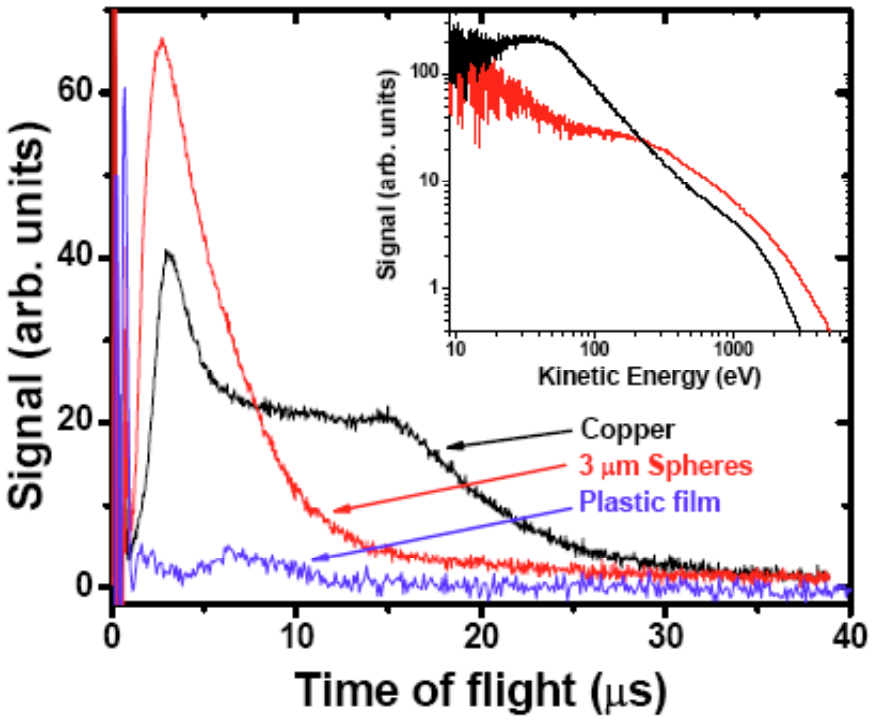

Figure I.F.4. Time-of-flight traces for polished copper targets and 2.9 μm sphere coated copper targets. (Inset) Kinetic energy spectra assuming Cu ions.

References for section I.F

1. S. P. Gordan, T. Donnelly, A. Sullivan, H. Hamster, and R. W. Falcone, Opt. Lett. **19**, 484 (1994).
2. G. Kulcsar, D. AlMawlawi, F. W. Budnik, P. R. Herman, M. Moskovits, L. Zhao, and R. S. Marjoribanks, Phys. Rev. Lett. **84**, 5149 (2000).
3. P. P. Rajeev, P. Taneja, P. Ayyub, A. S. Sandhu, and G. Ravindra Kumar, Phys. Rev. Lett. **90**, 115002 (2003).
4. T. D. Donnelly, M. Rust, I Weiner, M. Allen, R. A. Smith, C. A. Steinke, S. Wilks, J. Zweiback, T. E. Cowan, and T. Ditmire, J. Phys. B **34**, L313 (2001).
5. D. R. Symes, A. J. Comley, and R. A. Smith, Phys. Rev. Lett. **93**, 145004 (2004).
6. A. A. Andreev and J. Limpouch, J. Plasma Physics **62**, 179 (1999).
7. E. L. Clark, K. Krushelnick, M. Zepf, F. N. Beg, M. Tatarakis, A. Machacek, M. I. K. Santala. I. Watts. P. A. Norreys, and A. E. Dangor, Phys. Rev. Lett. **85**, 1654 (2000).

I.G Laser heating of clusters

Participants:
M. Hohenberger, D. R. Symes, K. W. Madison A. Sumeruk, M. Teichmann, K. Hoffman J. Keto and T. Ditmire (University of Texas)

We have an ongoing campaign to study high intensity laser interactions with exploding clusters. During the past year, with support from the Center, we have performed two activities in this area: we have studied the explosion of heteronuclear clusters and we have begun the construction of an experiment that will allow us to irradiate clusters with intense short wavelength (100-10 nm) femtosecond pulses generated by the laser. This second activity is in the early construction phases. However, we have had good success in study of exploding mixed species clusters.

Our work has been motivated by a series of results published in recent years. Over the last several years, there has been much activity in studying high intensity, ultrashort laser pulse interactions with atomic clusters. At high intensity ($>10^{16}$W/cm^2) the physics governing the laser cluster interaction is fundamentally different than in previous optical studies on clusters. Femtosecond pulses are comparable to or shorter than the disassembly times of a cluster in the laser field and so the entire laser pulse interacts with an inertially confined body of atoms. The most dramatic consequence of this unique interaction has been the observation of high charge states and very fast ions [1-3]. As discussed in section I.D the ejection of ions with many keV of energy from exploding clusters can be exploited to drive nuclear fusion [4-7]. The vast majority of studies have centered on single species homonuclear clusters such as van der Waals bonded rare gas or hydrogen clusters. However, our initial work with CD_4 clusters in the context of the fusion experiment described above has motivated a more detailed study of the explosion of mixed species clusters.

It is now well established that for large, high-*Z* clusters subject to intense IR, optical or VUV irradiation and moderate intensity, the space charge forces in the cluster prevent complete escape of electrons photoionized in the cluster. This forms a nanoplasma which exhibits a variety of collective electron oscillation effects [8,9]. In contrast, at high enough intensity, particularly in smaller, low-*Z* clusters, an ultrashort laser pulse can quickly strip the cluster of most of its electrons resulting in a pure Coulomb explosion. The ions expand by mutual repulsion in the fully ionized cluster sphere. In this simple picture, the ion kinetic energies are simply related to their initial potential energy at their equilibrium position in the cluster. This model has been very successful in explaining the ion energies observed in a number of experiments with low to mid-*Z* clusters [2,10].

With this developing understanding of laser driven explosions in homonuclear clusters, the question exists as to whether mixed species, heteronuclear clusters like CD_4, will behave in the same manner under intense ultrafast laser irradiation. Theoretical results suggest that explosions of clusters with mixed atomic species may be more complicated and exhibit some interesting differences [11,12]. Among other experiments, the irradiation of HI clusters at high intensity ($>10^{16}$W/cm^2) [13] have been investigated. However, the dynamics and interplay of the two ion species in such clusters have not been studied in any experiments. The motivation for studying Coulomb explosions of mixed species clusters has been advanced recently through molecular dynamic simulations by Last and Jortner which indicate that the energies of lighter deuterons from exploding heteronuclear clusters, like D_2O or CD_4, could be increased through a dynamical effect [11,12]. In general, if the kinematic parameter for species $A = q_A m_B / q_B m_A$, is greater than 1 (where q and m are the charge and mass of the light ion A and heavy ion B), then the light ions will outrun the heavier ions, exploding in an outer shell with a higher average energy beyond

what would be expected from the naïve estimate of ion energy based on initial potential energy as in the simple Coulomb explosion picture.

In our work this year, we performed an experimental confirmation of this dynamic enhancement of light ion energies from exploding heteronuclear clusters using methane (CH_4) and fully deuterated methane (CD_4). At the intensities used here ($\geq 10^{17}$W/cm^2) the C atoms in the cluster can be stripped to 4+ [12]. In this case $A = 1.5$ for CD_4 clusters whereas $A = 3$ for CH_4. Just considering the initial potential energy, the deuterons and protons from the same sized CH_4 and CD_4 clusters would acquire the same explosion energy upon irradiation. However, if the predicted kinematic enhancement of the light ion energies occurs, then the effect should be stronger in the case of CH_4 compared to CD_4 and be detectable through a study of these two molecular clusters under identical cluster formation and irradiation conditions. By comparing ion energy spectra we indeed observe a clear enhancement in the explosion energy of protons compared to deuterons.

In our experiment a pulsed supersonic gasjet with an orifice of 750 _m, directed through a skimmer produced a low density cluster beam. The energies of the ions created by the laser cluster interaction were determined by measuring the time of flight (TOF) of the ions in a field free drift tube of 1.14 m length. A microchannel plate (MCP) detected ions in an angular cone of $7.8\text{x}10^{-4}$sr from the focus. To estimate a mean cluster-size, we employed the Hagena parameter [14] $k \cdot p_0 \cdot (d/\tan\varepsilon)^{0.85}/T_0^{2.29}$ where ε is the expansion half angle ($\varepsilon = 5°$), T_0 and p_0 are the reservoir temperature and pressure and k is a constant related to the intermolecular bonding potential of the clustering gas. Assuming k=2360 [15] for both CH_4 and CD_4, the cluster size distribution for both gases is expected to be the same. A previous characterization [7] of a similar gas jet with an expansion half angle of ε=9.8° and operated with T_0=295 K and P_0=1000 psi found a mean CH_4 cluster size of 3 nm so with our settings of ε=5°, T_0=295 K and P_0=532 psi we also expect a cluster size of approximately 3nm. To irradiate the clusters we utilized the THOR laser. The laser was focused using an *f*/4.9 refractive graded index aspheric lens limiting the maximum energy to <0.1 J. The laser energy was measured after the output window of the vacuum chamber and so the values are an underestimate of the actual on-target energy. The energy was varied between 21 mJ and 70 mJ providing intensities between ~$9.6\text{x}10^{16}$W/cm^2 and ~$3.2\text{x}10^{17}$W/cm^2.

An example of a measured energy spectrum is shown in figure I.G.1. The original TOF data from which the spectrum was derived, using the formula $f(E) = f(t)\cdot(dE/dt)^{-1}$, is shown in the inset and was averaged over 200 laser shots. For the transformation of the time of flight signal to an energy spectrum we had to assume a certain mass, which we set to the mass of a proton or a deuteron, according to the gas we were shooting. The signal recorded by the MCP is a superposition from both carbon and deuterium/hydrogen arriving at the detector and these signals cannot be separated. However, we conducted simulations on the cluster explosions giving us information about the likely energy distribution for each particle species. The acquired results show, in good agreement with the simulations obtained in [12], that the maximum energy for carbon ions is approximately 2.5-3 times the maximum energy of the lighter species. We can determine a minimum time of flight for the heavier carbon ions which corresponds to a maximum energy in the obtained energy spectrum using the mass of the lighter ion species. Any signal above that energy is assumed to be caused by the detection of hydrogen or deuterium ions.

This characteristic energy is given by $E_{min} = E_C \cdot m_A/m_C$, where E_C is the maximum carbon energy and m_A and m_C are the light ion mass and the carbon mass respectively.

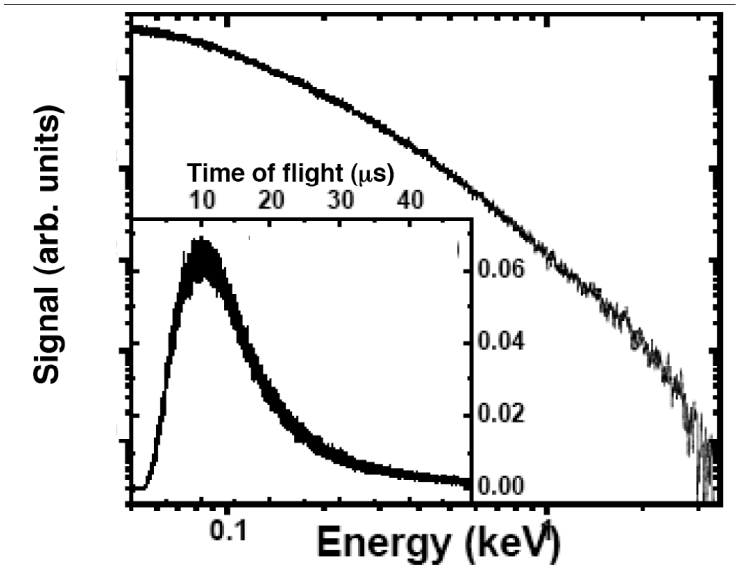

Figure I.G.1: Averaged energy spectrum and time of flight trace (inset) from CD_4 clusters irradiated at $2.1x10^{17}W/cm^2$.

Simulations of the dynamics of a driven electron cloud inside a cluster suggest that a cluster will be fully stripped of electrons by the laser field, if the ponderomotive potential is comparable to or larger than the surface potential of the charged cluster [16]. Therefore, for 3 nm methane clusters with the carbon atoms ionized to 4+, the laser intensity required to drive a pure Coulomb explosion can be estimated as $I \geq 1.4x10^{17}W/cm^2$, satisfied for the majority of our laser shots. Theoretical energy spectra for both homonuclear and heteronuclear [11] Coulomb explosions feature an increase in ion yield with energy up to a sharp cutoff determined by the potential energy of the ions at the surface. This shape of spectrum is not what we observe. We attribute this difference to the distribution of cluster sizes present in the gas expansion. As demonstrated previously, the convolution of a cluster size distribution function with a theoretical Coulomb explosion distribution results in a spectrum very similar in shape to the ones we have observed [5].

Figure I.G.2 shows kinetic energy spectra at different laser intensities, normalized using the original TOF traces, comparing CH_4 and CD_4 data. The low energy components of the spectra are not shown so the curves do not intersect. The energy ranges that we attribute solely to the lighter ion species are marked with dotted lines. Clearly the hydrogen energies always exceed the measured deuterium energies in the range presented here. This implies the validity of the theory predicting kinetic energy enhancement. An unexpected feature is that there seems to be a significant difference in maximum energy between the two species, increasing with higher laser intensity ranging up to a difference of almost 2 keV. The maximum energy is determined by the outermost particles in the cluster which therefore never experience the dynamic energy enhancement since they do not outrun any heavy ions and so should be unaffected by the species

chosen. However, it is likely that we do not actually detect the highest energy particles since their flux is so weak that the signal falls below the noise level. Hence the apparent separation of maximum energy could still be the effect of kinetic energy enhancement. Also unexpected is the increase of maximum ion energy with laser intensity since a pure Coulomb explosion is driven solely by ion repulsion forces and the laser conditions beyond the saturation intensity are irrelevant. This behavior could also be a consequence of a cluster size distribution since at the lower intensities the larger clusters may not be fully stripped of their electrons.

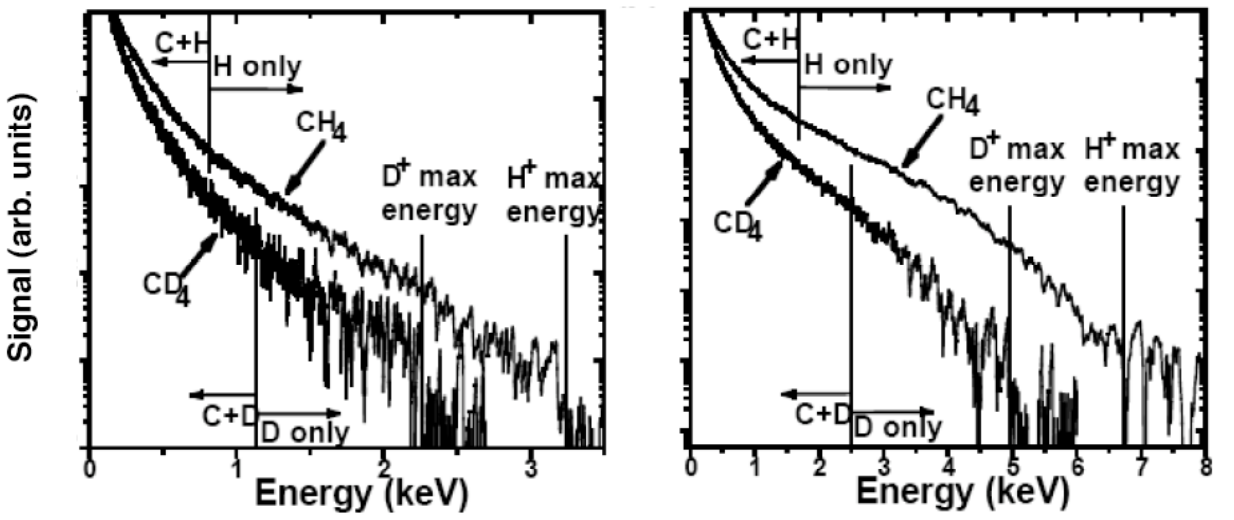

Figure I.G.2: Energy spectra from CH_4 and CD_4 clusters at a laser intensity of (left) $1.2x10^{17}W/cm^2$ and (right) $3.2x10^{17}W/cm^2$. Dotted lines indicate the regions where the signals are assumed to be solely due to the light ion species, H^+ or D^+.

With this experimental data we have clearly demonstrated the effect of kinetic energy enhancement in the Coulombic explosion of heteronuclear clusters as predicted in simulations by Last and Jortner [11,12]. In methane clusters, the average kinetic energy of the resulting hydrogen ions is significantly higher than the energy of deuterium ions under identical conditions. The importance of this kinematic enhancement for cluster-based short pulse neutron generation schemes is still under investigation.

References for section I.G

1. T. Ditmire *et al.*, Nature (London) **386**, 54-56 (1997).
2. M. Lezius *et al.*,Phys. Rev. Lett. **80**, 261-264 (1998).
3. V. Kumarappan, M. Krishnamurthy, and D. Mathur,Phys. Rev. Lett. **87**, 085005 (2001).
4. T. Ditmire *et al*. Nature (London) **398**, 489-492 (1999).
5. J. Zweiback *et al.*, Phys. Plasmas **9**, 3108-3120 (2002).
6. G. Grillon *et al.*,Phys. Rev. Lett. **89**, 065005 (2002).
7. K. W. Madison *et al.*, Phys. Plasmas **11**, 270-277 (2004).
8. T. Ditmire *et al.*, Phys. Rev. A **53**, 3379-3402 (1996).
9. U. Saalmann and J.-M. Rost, Phys. Rev. Lett. **91**, 223401 (2003).

10. S. Sakabe *et al.*, Phys. Rev. A **69**, 023203 (2004).
11. I. Last and J. Jortner, Phys. Rev. Lett. **87**, 033401 (2001).
12. I. Last and J. Jortner, J. Phys. Chem. A. **106**, 10877-10885 (2002).
13. J. W. G. Tisch *et al.*, Phys. Rev. A **60**, 3076-3080 (1999).
14. O. F. Hagena and W. Obert, J. Chem. Phys. **56**, 1793-1802 (1972).
15. R. A. Smith, T. Ditmire, and J. W. G. Tisch, Rev. Sci. Instrum. **69**, 3798-3804 (1998).
16. I. Last and J. Jortner, Phys. Rev. A **60**, 2215-2221 (1999).

I.H Ultrafast radial transport in a micron-scale aluminum plasma excited at relativistic intensity

Participants:
B.T. Bowes, M. C. Downer (University of Texas)
H. Langhof (Physikalisches Institut der Universität Würzburg)
M. Wilcox, B. Hou, J. Nees and G. Mourou (University of Michigan)

Under support from the Center, we have conducted a series of heat transport experiments in HED plasmas using a short pulse laser to heat a solid target. These experiments are, principally, a collaboration between Texas and Michigan

Intense, high contrast femtosecond laser pulses deposit energy into the electrons of a solid faster than it escapes from the initially-excited volume and much faster than the target surface expands hydrodynamically. When initial electron temperature kT_e exceeds several hundred eV radiative heat transport begins to dominate over collisional transport [1]. Past experiments in this regime [1] used loosely focused, ~1J, ~1ps pump pulses and probed the target transversely in transmission and thus were restricted to observing late stages of 1D radiative transport in an optically transparent material on a time scale of tens of picoseconds. Within our work over the last couple of years, we performed measurements using 1mJ, 24fs pump pulses from the kHz Ti:sapphire laser at the University of Michigan focused to a diffraction-limited □²-size spot (1.5μm diam.) to excite a metal target surface at relativistic intensity. We probe the target in reflection through microscope optics. This geometry enables us to observe the earliest stages of radiative transport in 2D on *any* target material on a sub-picosecond time scale. New features of radiative transport are expected on this space-time scale. For example, simple transport models in the diffusive limit (*i.e.* Rosseland radiation mean free path □$_R$ << heated spot size □) predict very different temporal evolution of the thermal/ionization front in 2D vs. 1D [3]. Moreover, since our focal spot size is on the order of □$_R$, our experiment may open up fs studies of *nonlocal* radiative transport.

Pump pulses, focused with an f/1 off-axis paraboloid coupled to adaptive optics [2], excite an Al target at 1kHz repetition rate. At the highest focused pump intensity, K□ and continuum bremsstrahlung x-rays are clearly observed. The target is translated so each laser shot interacts with clean target material. Surface wobble is limited to <1μm giving highly reproducible damage spots. The probe is split from the pump, frequency-doubled and focused at 60° incidence angle to a ~20μm spot centered on the pump spot. The reflected probe is imaged with high quality

microscope optics onto a CCD camera, recording 140× magnified images of the pump-excited spot with <1μm spatial resolution.

The darkening in the center of the target area (illustrated in figure I.G.1 a) indicates heating and ionization of the Al surface, but its physical origin must be understood to model transport quantitatively. In figure I.G.1 b we plot $\Delta R_{probe}(\Delta t)/R_0$ in P- and S- polarized probe reflectivity for excitation at 1.8×10^{18}W/cm^2 obtained by the measuring the center of the imaged pump-excited region. ΔR is negligible for an S-polarized probe showing that the drop of the P-polarized reflectivity is caused by resonance absorption (RA) [4] at the expanding critical surface. The critical surface expands vertically at the ion acoustic velocity and max. RA occurs when it expands to $v_z\Delta t_{max}\approx\lambda_{probe}/8\approx50$nm. [4]. From Fig.1b, $\Delta t_{max}\approx0.3$ps, implying $v_z\approx2\times10^7$cm/s. This v_z is consistent with ionization state $Z\approx10$ and $kT_e\approx$ several keV. The slight delay between ionizing and heating a point on the surface to (Z,kT_e) and the appearance of maximum RA must be taken into account in modeling the radial expansion data. Since vertical expansion $v_z\Delta t$ remains much less than the radial spot size during the time interval ($0<\Delta t<1$ps) of interest, a 1D hydrodynamic MEDUSA-like model [5] is sufficient. Although pre-pulses at the 10^{-5} level were present no ΔR_{probe} occurred before arrival of the main pump pulse.

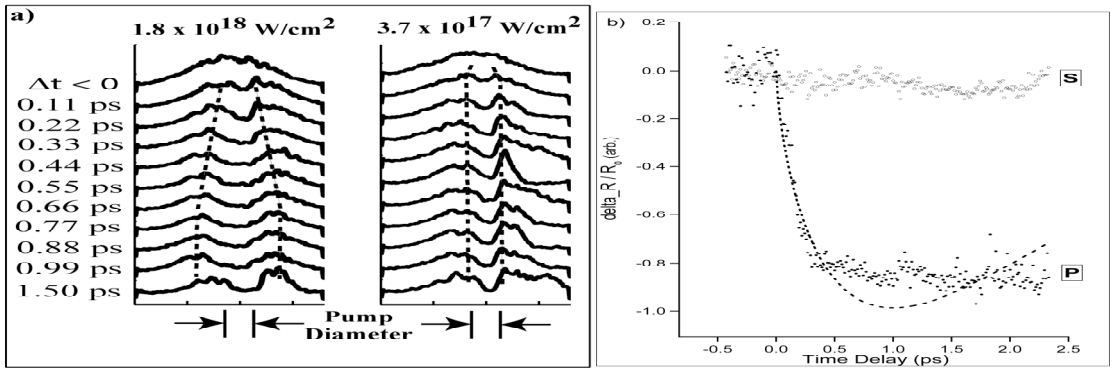

Figure I.G.1. a) Lineouts from probe images at two different pump laser intensities. Large radial expansion of the laser excited region is clearly observed at the highest pump intensity (left) but is nearly absent when the pump laser intensity is reduced to 3.7×10^{17}W/cm^2. b) Normalized S- and P-polarized probe beam reflectivity $\Delta R_{probe}(\Delta t)/R_0$ of the center of the laser excited region for pump intensity 1.8×10^{18}W/cm^2. Dashed curve: fit of P-polarized data to a 1D RA model [4] assuming constant vertical expansion velocity $v_z=2\times10^7$cm/s. The data deviate from the model for $\Delta t>1$ps because the critical surface expansion becomes 3D and kTe has cooled.

We model the evolution of the electron temperature profile $T_e(r, z\le0, t)$ at constant solid density ρ by numerically solving the nonlinear diffusion equation $\partial T_e/\partial t = \nabla\bullet(\kappa\nabla T_e)$ with a T_e-dependent thermal diffusivity $\kappa = (\kappa_{SH} + \kappa_R)/\rho c_v$ that included collisional (Spitzer-Härm) conductivity $\kappa_{SH} \sim (kT_e)^{5/2}/(Z+1)$ and radiative conductivity $\kappa_R = 16\sigma_{SB}T_e^3\lambda_R/3$ [3], where λ_R[cm] = $(9\times10^6)T_e[^oK]^2/Zn_e[cm^{-3}]$ is a simplified radiative mean free path for hydrogenic ions [1,3]. The initial condition was defined by partitioning absorbed pump energy (~1mJ, Gaussian radial profile) between electron thermal energy kT_e and ionization $Z(kT_e)$ assuming Saha equilibrium. The choice of initial absorption depth z_{abs} was not critical because $T_e(r,z\le0,t)$ quickly evolved to a nearly hemispherical profile which became the effective initial condition. Our code reproduces the 1D transport results of ref. [1]. We complete the model by coupling the calculated $T_e(r,z<0,t)$

to the 1D hydrodynamic model assuming $T_e(r,z>0,t)=T_e(r,0,t)$. This approximation is justified by the low heat capacity and high thermal conductivity of the expanding coronal plasma.

Figure I.G.2 shows the calculated profile of the critical surface S(r,z) at several Δt for excitation at 1.8×10^{18}W/cm^2. During 0<Δt<1ps, S expands vertically at nearly constant $v_z\sim2\times10^7$cm/s. Simultaneously it expands radially, at first rapidly, then rapidly decelerating because of the highly nonlinear □. The radius r_c of the "dark" spot was taken to be the radius of S(r,z) at $z=\lambda_{probe}/8$ (max. RA). The resulting time evolution $r_c(\Delta t)$ is plotted in Fig. 2b and compared with the measured HWHM $r_{dark}(\Delta t)$ of the dark spot.

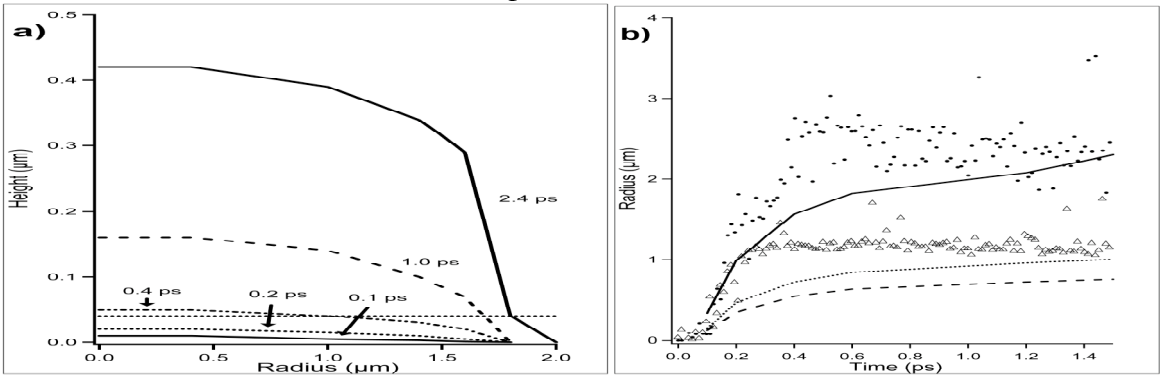

Figure I.E.2. a) Calculations of expanding critical surface of the laser-excited target from combining 2D radiative transport model with 1D hydrodynamic model at different times Δt. b) Data points: Measured radius $r_{dark}(\Delta t)$ of darkened pump-excited plasma region at pump intensities 1.8×10^{18}W/cm^2 (circles) and 3.7×10^{17}W/cm^2 (triangles). Curves: Calculated radius $r_c(\Delta t)$ of critical surface highest intensity (solid), lower intensity (dotted) and neglecting radiative transport (dashed).

Both curves reproduce the measured spatial extent of radial expansion quite well. The main discrepancy between measured $r_{dark}(\Delta t)$ and calculated $r_c(\Delta t)$ (inc. λ_R) is the faster initial evolution of the former. We believe that this is caused in part by the initially nonlocal character of the radiative transport, which cannot be described by a diffusion equation. This belief is based on an estimated $\lambda_R\sim1\mu$m, comparable to the pump focal spot size, for our estimated initial conditions. Additional complications may be the dependence of λ_R on material opacity, which has been greatly simplified in our model, and the transport of hot electrons by **E**×**B** drift. [6] The latter effect pulls electrons out of the corona into vacuum, moves them radially away from the plasma region then drives them back into cool target material.

References for section I.G

1. T. Ditmire *et al.*, "Supersonic ionization wave driven by radiation transport in a short-pulse laser-produced plasma," Phys. Rev. Lett. **77**, 498 (1996).
2. O. Albert *et al.*, "Generation of relativistic intensity pulses at a kilohertz repetition rate," Opt. Lett. **25**, 1125 (2000).
3. Y.B. Zel'dovich and Y.P. Raizer, *Physics of Shock Waves and High-Temperature Hydrodynamic Phenomena*, edited by W.D. Hayes and R.F. Probstein (Dover, New York, 2002)
4. W. L. Kruer, *The Physics of Laser-Plasma Interactions* (Addison-Wesley, 1988).

5. J.P. Christiansen *et al.*, "MEDUSA a one-dimensional laser fusion code," Comp. Phys. Commun. **7**, 271 (1974).
6. Y. Sentoku *et. al.*, "Laser light and hot electron micro focusing using a conical target," Phys. Plasmas **11**, 3083 (2004).

I.I Proton Acceleration

Participants:
A. Maksimchuk and D. Umstadter (University of Michigan)

Work at the University of Michigan was supported by a TCHILS subcontract to Prof. Umstadter. This work focused on proton acceleration from laser irradiated slab targets. We have an interest in proton acceleration as a means to generate a heating beam for warm-dense matter experiments. This work leverages the ongoing experiments at Michigan on proton accleration from solid slab targets irradiated by an intense laser pulse on the front surface. The presence of MeV protons from these interactions is well known and our work is aimed at optimizing their production with table top scale lasers

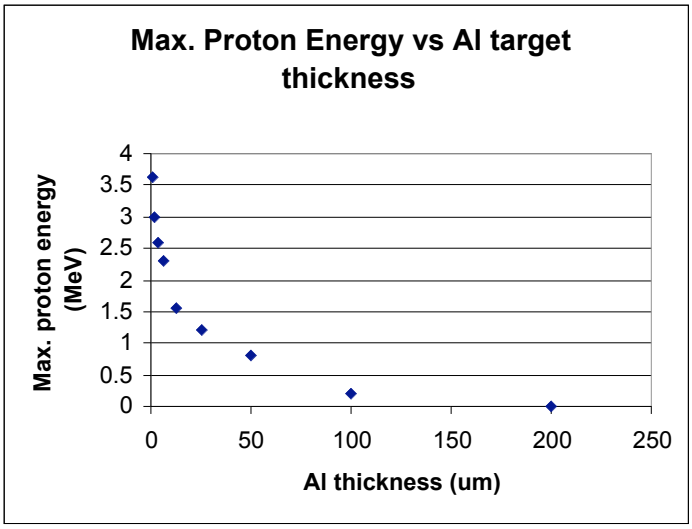

Figure I.I.1: Maximum proton energy vs target thickness of Aluminum targets

In order to optimize our laser-accelerated proton beam for high-energy-density physics experiments, the maximum proton energy vs target thickness of Aluminum was studied with frequency-doubled laser light at peak intensity 2.9×10^{19} W/cm^2 and a 3-μm FWHM focal spot using the Michigan T^3 laser. The relationship between maximum energy and target thickness found experimentally is shown in figure I.I.1. Reducing the target thickness, from 200μm to 0.8μm, results in an increasing maximum proton-energy. This result is markedly different from the 13-μm peak from experiments using 1-μm- fundamental wavelength laser light. Moreover, this is good evidence that the contrast after doubling is sufficiently high that no significant burn-

through effects occur with ultra-thin targets. The max proton energy vs peak intensity is also shown in figure I.I.2.

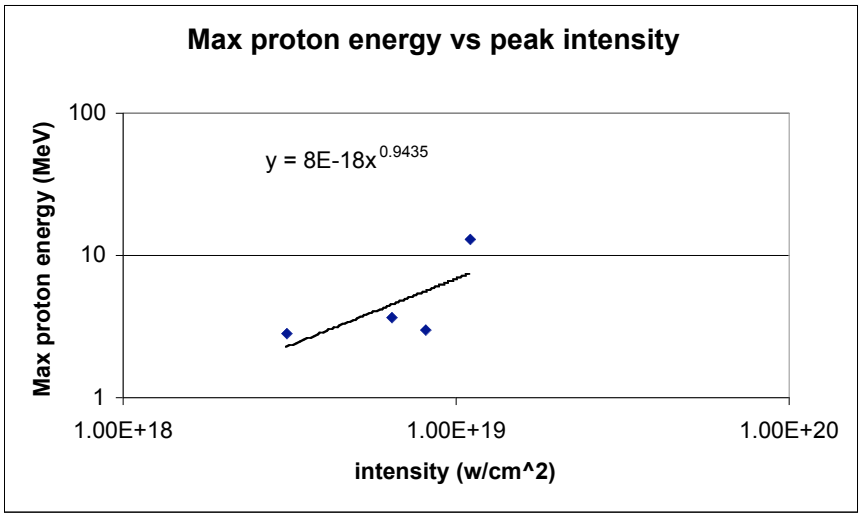

Figure I.I.2: Maximum proton energy vs peak intensity from Al targets

Each point in this plot is averaged from at least 10 shots. The purpose for this study is to find the intensity dependence of proton acceleration.

A study of the distribution of accelerated electrons from solid targets was also conducted. Radiographic film was installed around the target plate under the same conditions as the above experiments. It was observed that electrons, but not protons, were accelerated along the tangential direction, along the target plate. Electrons were also observed for the first time to be accelerated at an angle between the laser direction and the target normal. These novel effects are being further investigated and will form part of the basis for the second year's research. Also in the second year, a new 100-TW-laser facility is being constructed at the University of Nebraska, Lincoln, which will allow much more complete studies of these phenomena. Once the proton beam and electron beam are optimized, they will be used in high-energy-density studies, in support of the TCHILS program. It is also hoped that with lasers coming online both at Austin and Lincoln, better control of the laser scheduling for HEDP experiments will be permitted.

II. Texas Petawatt construction activities

The Center is also undertaking an extensive campaign of laser development, focusing on the development of the Texas Petawatt laser. Since these activities are described in detail elsewhere, we simply summarize them in this section. Greater details on the Texas Petawatt project can be found in the Texas Petawatt Conceptual Design Report.

I.A Design of the Texas Petawatt Laser

Participants:
E. W. Gaul, T. Ditmire, M. D. Martinez, S. Douglas, D. Gorski, G. R. Hays and W. Henderson (University of Texas)
A. Erlandson, J. Caird, C. Ebbers, I. Iovanovic, W. Molander (Lawrence Livermore National Laboratory)

Within TCHILS the development of a novel a petawatt laser has been proposed as the experimental core of the research center. The nature of many of the experiments proposed, require a pulse width near 100 fs. Also, pulse energies of between 100-300 J are desirable. Activity over the past year has included conclusion of the detailed design of the laser as well as initial procurements and construction.

In recent years a number of approaches to high energy chirped pulse amplification (CPA) have been explored. These recent advances in high intensity laser development were described this year at the International Conference on Ultrahigh Intensity Lasers (ICUIL) [1]. In particular, Nd;glass systems have been extremely successful in pushing CPA to the multi-joule level, as illustrated with the extreme scaling of CPA in Nd;glass by the LLNL Petawatt [2]. While Nd:glass is attractive because of the high quality, large aperture amplifiers that are possible, Nd:glass exhibits a rather limited gain bandwidth of about 10 nm. Additionally, gain narrowing further diminishes the spectral width of a broadband seed pulse and prohibits recompressed pulse widths much below one picosecond. Thus, a straightforward Nd:glass architecture is not appropriate for the laser parameters envisioned (200J/150FS). CPA with Ti:sapphire has been demonstrated with pulses down to 20 fs and several joules, and a number of groups worldwide are currently pushing Ti:sapphire lasers to the multi-hundred TW level by increasing the energy and crystal size. Despite the broad bandwidth available, Ti:sapphire's largest disadvantage for high energy systems is that the short excited state lifetime of Ti:sapphire (3.2 μs) demands that it be pumped by a second laser operating in the green (such as the second harmonic of a ns Nd:YAG or Nd:glass laser). Although gain narrowing is not as significant in Ti:sapphire, the gain per pass is very limited at the peak fluorescence of Nd:glass. Ultimately, crystal size, and the cost of pump laser prohibit this approach for the Texas Petawatt Laser.

To push the pulse width limit attainable in Nd:glass laser systems, a hybrid approach will be taken, which uses a broadband amplification for the majority of the system gain (10^9) up to the joule level and then Nd:glass amplifiers are used to extract the bulk of the energy with an overall gain approximately 10^2. The principal approach of the Texas Petawatt laser is to use OPCPA, which is more flexible in selecting a gain maximum. Also, operating at least one OPCPA stage in saturation can increase the bandwidth of the seed pulse. After more than nine orders of magnitude net gain in OPCPA, the bandwidth will effectively broaden. More than 99% of the energy with a gain of <300 will be extracted out of Nd:glass amplifiers. By balancing the gain between silicate and phosphate Nd:glass a final bandwidth of 10-12 nm can be reached leading to compressed pulsewidths of 150-170 fs.

Figure II.A.1 displays a schematic layout of the laser system. A Ti:sapphire oscillator produces 100 fs pulses at 1057 nm. The pulses are stretched to 1.8 ns (GDD = 115 ps/nm) by double

passing (8 grating reflections) a compact, folded stretcher. The stretcher is a modified Banks stretcher ref [2], which replaces the mirror stripe on the grating with a stripe mirror mounted in front of the grating to allow a higher bandwidth transmission for a smaller size grating. The pulses then pass through a Dazzler to correct phase distortions and to pre-shape the spectrum. After a Pockels cell slicer the 10 Hz pulses are amplified in two OPCPA stages, which are pumped by a commercial 8 ns, 1.2 J Q-switched laser with a top hat spatial profile. The first stage uses three 15 mm long BBO crystals with walk-off compensation and a gain of ~100 per crystal. The second stage uses a walk-off compensated pair of BBO crystals with a saturated total gain of ~100 and an output bandwidth > 30 nm. Figure II.A.2 illustrates spectral modeling results of the different amplifier stages. Such an OPCPA laser has been demonstrated [ref 2] and it was found that reducing the gain per crystal and simply adding additional crystals for the system net gain improved the reliability of the amplifier which allows the use of commercial Q-switched lasers for pumping. Using a commercial pump laser offers reduced complexity and price for pumping OPCPA. The output of these stages will be ~50-100 mJ and the bandwidth is limited by the size of the stretcher optics to < 42 nm. A serrated aperture in combination with a spatial filter shapes the beam to an 8^{th} order super-Gaussian profile. The spatial profile is also slightly truncated on the sides to match the compressor clear aperture given by the grating size.

A third OPCPA stage then increases the energy to 0.5 J. This stage will use a single crystal and requires a custom pump laser that produces about 4 J in 4 ns with spatially and temporally flat pulses. The costly energy of the pump pulse will be used more efficiently by directing the unconverted green photons to pump a Ti:sapphire crystal after the OPA. A four pass amplification in Ti:sapphire with a gain G_0 ~1.3 per pass boosts the energy to 1 J. At this point the pulse duration is ~3.5 ns.

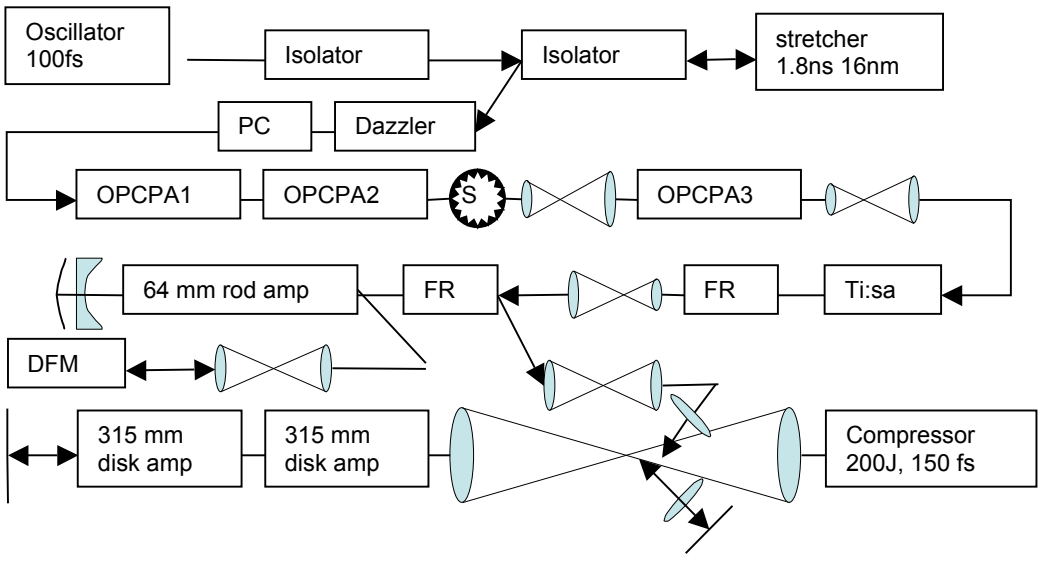

Figure II.A.1: Block diagram of the laser chain. PC is a slicer Pockels cell, DFM is a deformable mirror for wavefront correction, FR are Faraday rotators, SA is a serrated aperture.

The 1J pulse is then injected into a passive 4-pass through a 64 mm diameter, 240 mm long rod amplifier with silicate Nd:glass and yields an output energy of 31 J with a B-integral less than

0.5 radian. The Faraday rotator used for passive switching also ejects back reflections from the main amplifiers. The final stage is a 4-pass in a pair of 315 mm NOVA amplifiers, which contain two phosphate Nd:glass disks in each amplifier. The four passes are separated by angular multiplexing and are isolated with pinholes. About 400 J can be extracted out of these disks with an additional B-integral of only 0.25 radians due to the large beam size. However, the energy extracted will be limited to about 300 J due to the peak fluence limitations on the final grating. After the final pass through an amplifier disk the pulses are relay imaged into the compressor. The design goals for the individual amplifier stages are summarized in table II.A.1.

Table II.A.1 Designs goal for various stages of the laser chain.

Amplifier Stage	Energy [J]	Pulsewidth [ns]	Spectral Bandwidth [nm, FWHM]	ΦB	Beam Size [mm]
oscillator	10^{-9}	100 fs	16.4		3 (Dia.)
OPCPA2	.050	3.5	33		8 (Dia.)
Ti:sapphire	.80	3.5	33	.01	12 (Dia.)
rod amplifier	31	1.58	12.5	.50	45x55
2^{nd} pass disk	90	1.72	14.7	.55	180x220
4^{th} pass disk	250	1.47	12.4	.80	180x220
compressor	200	150 fs	12.0	.80	180x220

The double pass compressor uses a pair of 40x80 cm multilayer dielectric coated gratings with 1740 lines/mm at 124 cm separation and 73.2 degree angle of incidence. The input mirror has a vertical tilt of 0.65 degrees to separate the input and output beam and the rooftop mirror is replaced by a 0 degree mirror. The footprint of the incident and outgoing beam on the grating partially overlap which effectively increases the clear aperture though the compressor in the vertical dimension by up to 50 % reducing the fluence on the gratings. The damage fluence of the dielectric gratings is currently not well known for pulses as short as 150 fs. An operational fluence of just below 1 J/cm^2 in the beam is anticipated as reasonable. The vertical spatial chirp resulting from the tilt is negligible. The serrated aperture matches the beam size to the compressor's clear aperture and defines an image plane, which will be relay imaged throughout the chain.

One image plane will be at the deformable mirror after the second pass in the rod amplifier. A second image will be before the injection into the disk amplifier, where a static phase plate can be inserted to correct for wave front aberration of the lenses. Aberrations are induced by passing off axis though the lenses in the disk amplifier section, which also requires a meniscus lens close to the Nd:glass disk to avoid critical ghost foci. Large lenses introduce besides the wave front distortions a significant amount of spatial group delay chirp and spatial group delay dispersion chirp [4]. The center of the beam passes through an additional ~4 cm of lens glass material

compared to the edge of the beam, which leads to additional 1.3 ps group delay at the center and additional group delay dispersion broadens the pulse by 40 fs at the center of the beam. Both effects can be reduced by using achromatic lenses or by inserting extra material at the edge of the beam which can be done by replacing the mirror at the rod amplifier with a negative lens and a curved mirror.

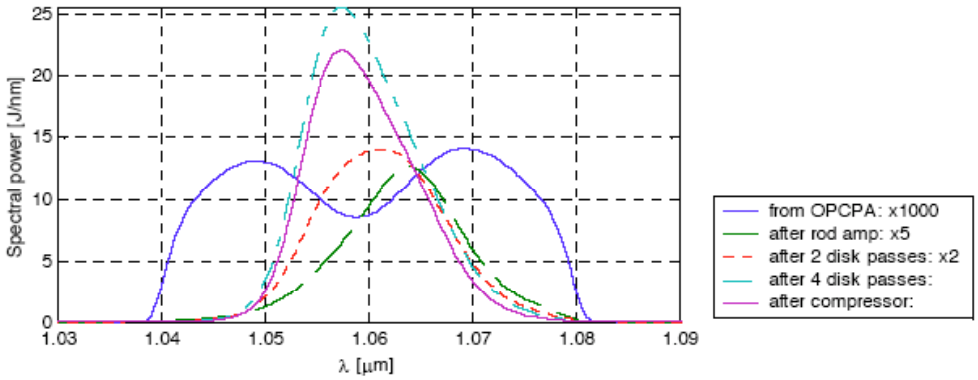

Fig. II.A.2 *Normalized spectral power after several amplifier stages*

The laser is constructed inside a 1600 sqft, class 100,000 cleanroom and will be assembled on a 180 sqft optical table. The compressor which is fits on a 5x8' breadboard inside a vacuum vessel will be installed outside the cleanroom in the target area near two target chambers which are enclosed by a concrete brick wall for radiation shielding. The capacitor storage bank and the pulsed power equipment for the disk amplifiers are located in a separate room. A full system shot sequence will be initiated remotely in a separate control room with a full suite of controls and diagnostics systems interface.

When the facility (figure II.A.3) is fully commissioned in 2007, the Texas Petawatt will also employ a long pulse laser (500J, 532nm @ 1-20ns) not described in this paper. This high energy (500 J), long pulse (1-20 ns), synchronized laser is proposed to complement the Texas Petawatt Laser. The combination of this short pulse laser with a second long pulse laser beam enables an even greater range of high energy density studies.

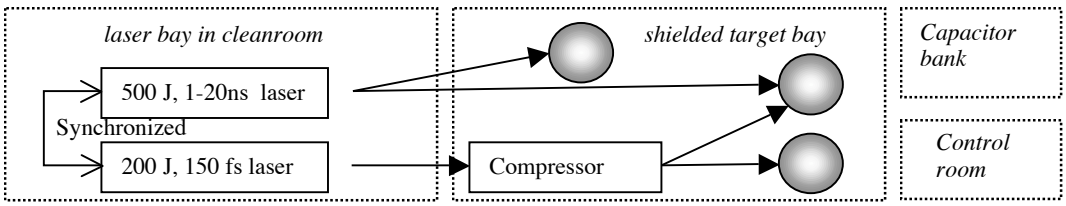

Fig.3 Schematic overview of the Petawatt facility.

References for section II.A

1. International Conference on Ultrahigh Intensity Lasers 2004, Tahoe City, CA
2. M. Perry, *et al*, Opt. Lett. 24, 160 (1999)
3. I. Jovanovic, *et. al,* Applied Optics, **41**, 2923-2929, 2002
4. Z. Bor, Journal of modern Optics, **35**, 1907-1918, 1988

II.B Spectral shaping efforts to achieve near 100 fs pulses from a hybrid OPCPA and mixed Nd:glass amplifier

Participants:
G. R. Hays, E. Gaul, and T. Ditmire *(University of Texas)*

In addition to the central Petawatt laser development, we have undertaken a smaller scale project that will assess the technology needed to make the Petawatt laser pulses shorter than 200 fs. To do this, we have initiated the construction of a 10 TW scale, hybrid OPCPA/mixed Nd:glass laser. Work this past year has focused on the construction of the front end of this system.

This work is motivated by the fact that CPA and the development of high intensity laser systems have been primarily limited to two laser host mediums, Titanium sapphire and Neodymium doped laser glass. Ti:sapphire systems have allowed the development of ultrashort pulses (<30 fs) due to its broad spectral emission. However it is limited by its relatively short fluorescence lifetime making it difficult to generate pulses exceeding a few joules. Nd:glass systems have been successful in pushing CPA to the multi-joule level. The availability of high quality, large aperture amplifiers has made it extremely attractive for high energy applications. However, its chief detractor is its limited spectral emission of 25 nm (FWHM). This limits the amplification of laser pulses with recompressed pulse widths of approximately 1 ps because gain narrowing significantly diminishes the spectral width of the seed.

In order to decrease the pulse width in glass lasers, hybrid systems utilizing Ti:sapphire and Nd:glass have been successfully deployed [1]. Here Ti:sapphire is used both to generate the seed and for preamplification to the several mJ level. The remaining bulk amplification is done in Nd:glass. At 1053 nm Ti:sapphire has extremely low gain making preamplification difficult. In addition the short excited state lifetime leads to rather extensive amplified spontaneous emission (ASE). This in combination with the limited spectral content of Nd:glass allows for compressed pulses of approximately 400 fs.

The recent development of optical parametric chirped pulse amplification (OPCPA) has spurred a great new interest in high intensity laser development [2]. OPCPA possesses and extremely broad and uniform gain spectrum. Gains in excess of 10^3 over a broad spectrum have been achieved [3]. However, OPCPA is highly nonlinear and requires a strictly uniform pump pulse. This highly formatted pump pulse makes it costly and difficult to achieve amplified energies in excess of 1 J. Further hybrid techniques have utilized the shifted spectral lines of Nd:phospate and Nd:silicate glass [4,5]. The peak emission lines of phosphate and silicate glasses are separated by 8 nm and overlap nicely. By using a mixed glass amplifier chain, a broader gain

spectrum is available permitting amplified pulses with up to 16 nm (FWHM). This corresponds to a transform limited Gaussian pulse of 100 fs.

Our efforts have been to produce a hybrid CPA laser system utilizing all three of the previously mentioned techniques. We are developing a unique CPA laser that will combine the laser mediums of Ti:sapphire, OPCPA, and mixed laser glasses in an effort to maintain an amplified spectrum of up to 16nm FWHM. The use of each media in careful balance of gain allows us to develop a several Joule laser pulse with enough bandwidth to achieve a 150 fs in the transform limit.

In order to produce a near 150 fs compressed pulse from a Nd:glass amplifier chain, precision control of the pulse spectrum must be maintained. The natural emission of Nd:phosphate and Nd:silicate laser glasses are each in excess of 25nm FWHM and their peak spectral emissions are separated by 8 nm (Figure.II.B.1 a). Therefore by employing both media in an amplifier chain, the seed pulse experiences a net broader gain spectrum allowing us to reduce the effects of spectral gain narrowing. However the combined gain spectrum is still highly shaped and significant spectral narrowing will occur if the net gain is too high. Our system is designed to limit the gain from glass to 10^2 in the final amplification. Here high energy is achieved by the large energy storage capacity from the laser glass host. There the preamplification is done in a multi-stage OPA.

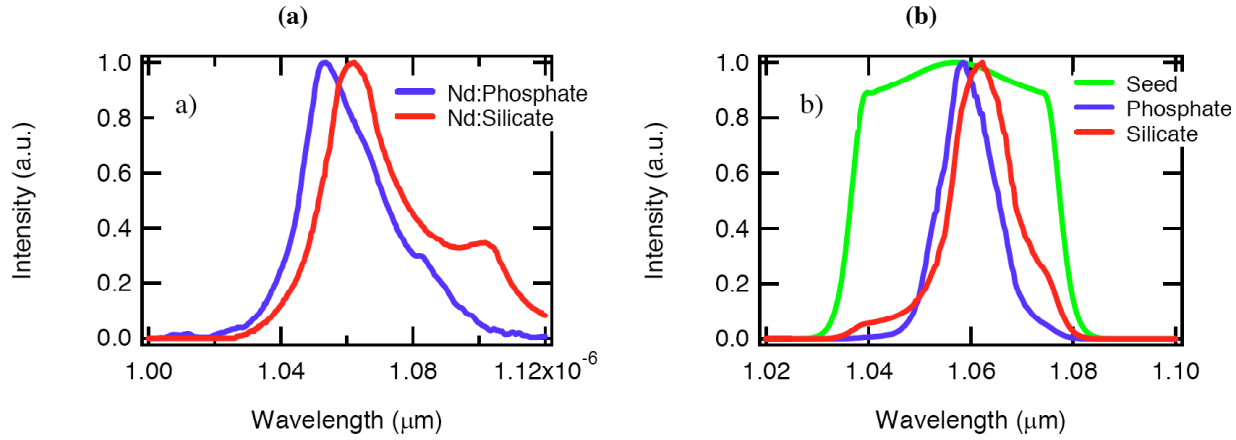

Fig II.B.1. Characteristics of phosphate and silicate laser glasses: (a) spectral emissions of Nd:phosphate and Nd:silicate laser glass, (b) simulated spectral shaping by amplifying a broadband OPCPA seed in a mixed laser glass amplifier chain. The seed is first amplified in Nd:silicate and then secondly in Nd:phosphate.

The benefits of OPCPA are pertinent to our design. Degenerate parametric amplification is inherently broadband. A nearly uniform gain spectrum over a 100 nm bandwidth with a gain of 10^3 is available from a singly passed nonlinear optical crystal. The detractor however is the highly nonlinear intensity dependent gain of the pump pulse. In order to achieve a uniformly amplified seed, the pump pulse must be both temporally and spatially uniform during the parametric interaction. Therefore an 8 ns, super-Gaussian pump pulse is used. The 1 ns seed is interacted with pump at the temporal peak to where it experiences nearly uniform intensity. Finally gain saturation in such a highly nonlinear medium allows for significant spectral broadening.

The nearly uniform spectrally broadened pulse from the OPA is then seeded into the mixed glass amplifier. Each rod is double passed to allow for efficient energy extraction. However the gain from phosphate and silicate laser glass is not the same. Phosphate glass has a smaller emission cross-section creating a larger small signal gain. Also, silicate glass has a broader spectrum that extends much further into red side of the spectrum. Therefore there exists a natural balance between the two combined gains that produces the largest amplified spectrum. Figure 1b shows our modeling simulations of a mixed glass amplifier. We will present preliminary gain measurements that demonstrate the spectral shaping of a mixed glass amplifier chain.

The laser system is designed by employing a Ti:sapphire based oscillator, an OPCPA preamplifier, and a mixed Nd:glass rod amplifier chain (Figure II.B.2). Our laser system utilizes a commercial Kerr-lens mode-locked, Ti:sapphire oscillator that produces 100 fs pulses with 16 nm of bandwidth (FWHM). The pulse train is then sliced down to 10 Hz and injected into an all-reflective single grating pulse stretcher producing a 1 nJ, 1 ns stretched seed pulse. A 3-stage nearly degenerate OPCPA chain is used for preamplification. Each BBO crystal is pumped by a frequency doubled Nd:YAG laser that is injection-seeded to eliminate temporal mode beating. The design goal is produce a >50 mJ pulse that is spectrally broadened by gain saturation in the OPAs.

Preliminary modeling suggests that if gain saturation is sufficiently achieved in the final OPA, the pulse will be spectrally broadened to >35 nm FWHM. Finally the pulse is double-passed in each of two 19mm diameter, 250 mm long Nd:glass rod amplifiers. The first head contains Nd:silicate and the second with Nd:phosphate. Each rod can store up to 30 J of energy. However the gain will be precisely managed to maximize the net spectral content and limit the B-integral. Finally the pulse will be compressed using a vacuum based, two grating pulse compressor. The dielectric compressor gratings are each ruled to 1740 lines/mm on a 35 cm by 15 cm substrate.

References for section II.B

1. M. D. Perry and B. W. Shore " Petawatt Laser Report" LLNL Internal report UCRL-ID-124933.
2. I.N. Ross, P. Matousek, M. Towrie, A.J. Langley, J.L. Collier, Optics Comm. **144**, 125-133 (1997).
3. I. Jovanovic, B.J. Comaskey, C.A. Ebbers, R.A. Bonner, D.M. Pennington, M.C. Morse, Appl. Opt. **41**, 2923-2929 (2002).
4. R. Danielius, A. Piskarsus, D.Podenas and A. Varanavicius, Optics Comm. **84**, 343-345 (1991).
5. N. Blanchot, C. Rouyer, C. Sauteret and A. Mingus, Opt. Lett. **20**, 395-397 (1995).

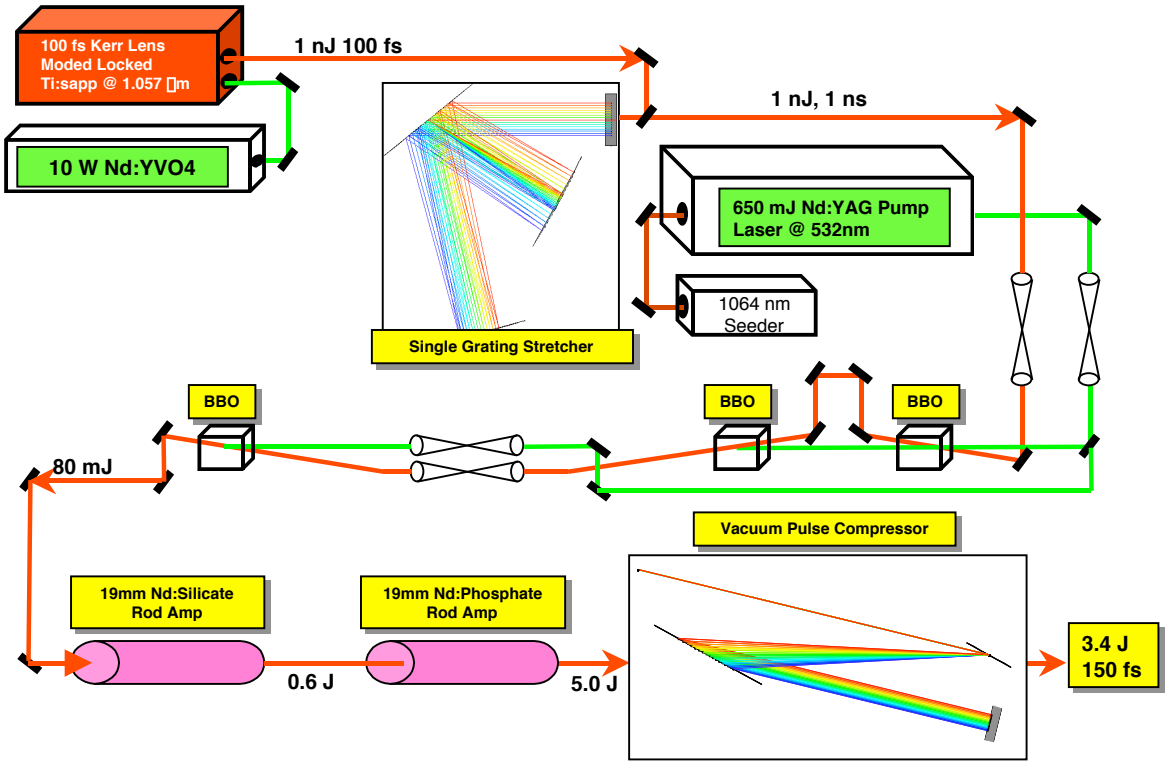

Figure I.B.2. Schematic of OPCPA and mixed Nd:phosphate and Nd:silicate laser.

III. Supporting Material

III.A Publications resulting from or supported by this NNSA SSAA Center Cooperative Agreement to date

1) A. D. Edens, T. Ditmire, J. F. Hansen, M. J. Edwards, R.G. Adams, P. Rambo, L. Ruggles, I.C. Smith, and J. L. Porter, "Study of hydrodynamic perturbations on high Mach number blast waves" *Phys. Rev. Lett.* Submitted.

2) R. Hartke, D. R. Symes, F. Buersgens, T. Ditmire, "Neutron Detector Calibration using a table-top laser heated plasma neutron source" *Rev. Sci. Inst.* Submitted.

3) J. F. Hansen, G. Luca, D. Froula, M. J. Edwards, A. E. Edens and T. Ditmire "Observation of a second shock formation in a radiative blast wave" *Phys. Rev. Lett.* Submitted.

4) W. Grigsby, A. Dalton, B. Bowes, S. Bless, J. Colvin, E. Taleff, M. Marder, M. Downer, T. Ditmire "Study of laser driven shocks in thin tin slabs" *J. Appl. Phys* in preparation.

5) B. T. Bowes, H. Langhoff, M. C. DOWNER, M. Wilcox, B. Hou, J. Nees and G. Mourou, "Femtosecond microscopy of radial transport in a micron-scale Al plasma excited at relativistic intensity," in preparation for *Phys. Plasmas* (2005).

6) M. Hohenberger, D. R. Symes, K. W. Madison, A. Sumeruk, and T. Ditmire, "Dynamic Acceleration Effects in Explosions of Laser Irradiated Heteronuclear Clusters", *Phys. Rev. Lett.* Submitted

7) K. W. Madison, R. Fitzpatrick, P. K. Patel, D. Price, T. Ditmire, "The role of laser pulse duration in Coulomb explosions of deuterium cluster targets" *Phys. Rev. A* **70**, 053201 (2004).

8) A. D. Edens, T. Ditmire, J. F. Hansen, M. J. Edwards, R.G. Adams, P. Rambo, L. Ruggles, I.C. Smith, and J. L. Porter, "Study of high Mach number laser driven blast waves" *Phys. Plas.* **11**, 4968 (2004).

9) L. E. Ruggles, J. L. Porter, W. W. Simpson, M. F. Vargas, D. M. Zagar, R. Hartke, F. Buersgens, D. R. Symes, T. Ditmire, "High sensitivity neutron detector for Z" *Rev. Sci Inst.* **75**, 3595 (2004).

10) T. Ditmire, S. Bless, G. Dyer, A. Edens, W. Grigsby, G. Hays, K. Madison, A. Maltsev, J. Colvin, M. J. Edwards, R. W. Lee, P. Patel, D. Price, B. A. Remington, R. Sheppherd, A. Wootton, J. Zweiback, E. Liang and K. A. Kielty, " Overview of future directions in high energy-density and high-field science using ultra-intense lasers" *Rad. Phys. And Chem.* **70**, 535 (2004).

11) K. W. Madison, P. K. Patel, D. Price, A. Edens, M. Allen, T. E. Cowan, J. Zweiback, and T. Ditmire, "Fusion neutron and ion emission from laser induced explosions of deuterium and deuterated methane clusters" *Phys. Plas.* **11**, 270 (2004).

12) B. T. Bowes, M. C. Downer, H. Langhoff, M. Wilcox, B. Hou, J. Nees and G. Mourou, "Ultrafast Radial transport in a micron-scale aluminum plasma excited at relativistic intensity," in *Advanced Accelerator Concepts*, *AIP Conference Proceedings* **737**, 609-613 (2004). Presented at 11th Advanced Accelerator Concepts Workshop, Stony brook NY, 23 June 2004.

13) R. Zgadzaj, E. W. Gaul, N. H. Matlis, M. C. DOWNER, and G. Shvets," Femtosecond pump-probe study of preformed plasma channels," *J. Opt. Soc. Am. B* **21**, 1559-1567 (2004).

14) B. Shim, G. Hays, M. Fomytskyi, A. Arefiev, B. Breizman, T. Ditmire and M. C. DOWNER, "Time-resolved harmnonic generation from exploding noble-gas clusters," in *Advanced Accelerator Concepts*, *AIP Conference Proceedings* **737**, 777-782 (2004). Presented at 11th Advanced Accelerator Concepts Workshop, Stony brook NY, 22 June 2004.

15) M. Fomytskyi, C. Chiu, F. Grigsby and M. C. DOWNER, "Controlled plasma wave generation and particle acceleration through seeding of the forward Raman instability," *Phys. Plasmas* **12**, 023103 (2004).

16) C. Chiu, M. Fomytskyi, F. Raischel, F. Grigsby, M. C. DOWNER and T. Tajima, "Laser accelerators for radiation medicine: a feasibility study," *J. Med. Phys.* **31**, 2042-2052 (2004).

17) A. Maltsev and T. Ditmire, "Above Threshold Ionization in Tightly Focused, Strongly Relativistic Laser Fields" *Phys. Rev. Lett.* **90**, 053002 (2003).

18) K. W. Madison, P. K. Patel, M. Allen, D. Price, T. Ditmire, "An investigation of fusion yield from exploding deuterium cluster plasmas produced by 100 TW laser pulses" *J. Opt. Soc. Am. B* **20**, 113 (2003).

19) G. Dyer, R. Sheppherd, J. Kuba, E. Fill, A. Wootton, P. Patel, D. Price, T. Ditmire, "Isochoric heating of solid aluminium with picosecond X-ray pulses," *J. Mod. Opt.* **50**, 2495 (2003).

20) J. Kuba, A. Wootton, R. M. Bionta, R. Shepherd, E. E. Fill, T. Ditmire, G. Dyer, R. A. London, V. N. Shlyaptsev, J. Dunn, R. Booth, S. Bajt, R. F. Smith, M. D. Feit, R. Levesque, M. McKernan, "X-ray optics research for free electron lasers: study of material damage under extreme fluxes," *Nuc. Inst. Meth. A – Accelerators, Spectrometers Detectors and Associated Equipment* **507**, 475 (2003).

21) J. F. Hansen, M. J. Edwards, H. F. Robey, A. Miles, D. Froula, G. Gregori, A. E. Edens and T. Ditmire "Laboratory Simulations of Supernova Shockwave Propagation and ISM Interaction" in *Inertial Fusion Science and Applications 2003,* Proceedings of the American Nuclear Society (2004).

22) J. Kuba, Wootton, A.; Bionta, R.M.; Shepherd, R.; Fill, E.E.; Dunn, J.; Smith, R.F.; Ditmire, T.; Dyer, G.; London, R.A.; Shlyaptsev, V.N.; Bajt, S.; Feit, M.D.; Levesque, R.; McKernan, M.; Conant, R.H., "X-ray optics research for linac coherent light source: interaction of ultra-short x-ray pulses with matter" in *AIP Conference Proceedings: 8th International Conference on X-Ray Lasers* vol **641**, p.596 (2002).

23) H.-K Chung; Fournier, K.B.; Edwards, M.J.; Scott, H.A.; Cattolica, R.; Ditmire, T.; Lee, R.W., "X-ray optics research for linac coherent light source: interaction of ultra-short x-ray pulses with matter" in *AIP Conference Proceedings: Atomic Processes in Plasmas* vol **635**, p.52 (2002).

III.B Students and Post Docs supported on this cooperative agreement

Project Participants	**Percentage of Time of Support (Based on 12 mos.)**	*Period of Appointments*
Undergraduates (Part/Time)		
Appolito, Brett W.		
Casares, Cristobal	2.1	02/23 - 03/21/04
Christiny, Nicolas	9.1	01/20 - 05/17/04
Gonzales, America	9.4	01/20 - 05/31/04
Landry, Jamie	23.4	01/20 - 08/31/04
Wu, Xi	4.7	05/15 - 06/30/04
	9.4	01/26 - 05/31/04
Graduate Research Assistant		
Bowes, Benjamin		
Brady, Parrish	62.5	01/16 - 08/31/04
Buersgens, Federico	45.8	09/01 - 05/31/04, 06/01 - 06/30/04
Cho, Byoung/ick	8.3	12/01 - 12/29/03
Churina, Irina	29.2	02/16 - 05/31/04
Dalton, Douglas	37.5	02/16 - 06/30/04
Dyer, Gilliss	8.3	06/01 - 06/30/04
Edens, Aaron	66.6	10/01 - 05/31/04
Flagg, Edward	37.5	02/16 - 06/30/04
Grigsby, Will	37.5	01/16 - 05/31/04
Hartke, Rene	37.5	02/16 - 06/30/04
Hays, Greg	45.8	10/27 - 12/31/04, 02/16 - 06/30/04
Hohenberger, Matthias	45.8	01/16 - 06/30/04
Keely, Sean	8.3	06/01 - 06/30/04
Maltsev, Alex	4.2	06/01 - 06/15/04
Morgan, Robert	8.3	02/16 - 02/29/04
Murphy, Brenden	8.3	06/01 - 06/30/04
Niemczura, Jonathan	8.3	06/01 - 06/30/04
Osterhoff, Jens	37.5	02/16 - 06/30/04
Sumeruk, Ariel	8.3	06/01 - 06/30/04
Zgadzaj, Rafal	29.2	02/16 - 05/31/04
	62.5	01/19 - 08/31/04
Postdocs		
Symes, Dan		
	58.3	02/01 - 08/31/04
Technical Staff		
Campbell, Jay		
Carter, Keith	83.3	11/01 - 08/31/04
Douglas, Skyler	25.0	03/01 - 08/31/04
Hoffman, Kay	4.2	08/23 - 08/31/04
Martinez, Mikael	50.0	03/01 - 08/31/04
	37.5	04/19 - 08/31/04
Researchers		
Ditmire, Todd, P.I.		
Gaul, Erhard	8.3	08/16 - 8/31/04
	83.3	11/01 - 8/31/04
Administrative		
Stewart, Saralyn		
	8.3	12/01 - 12/31/04